HAMILTON COLLEGE SENIOR FELLOWSHIP

ROTATIONAL ENERGY TRANSFER AND RELAXATION OF ELECTRONICALLY-EXCITED NITRIC OXIDE IN ATMOSPHERIC FLAMES AND FLOW CELLS

Félix Fernández-Alonso
Hamilton College Senior Fellow

Thesis submitted to the Faculty of Hamilton College in partial fulfillment of the requirements for the degree, Bachelor of Arts

1994

Certification of approval:

_____
Professor George A. Raiche
Principal Advisor

_____
Professor Ann Silversmith
Co-Advisor

ABSTRACT

This work reports laser-induced fluorescence measurements of rotational energy transfer (RET) in the $A\text{-}^2\Sigma^+$ Rydberg state of NO in atmospheric flames and in a room-temperature flow cell for N_2 and CO_2. The flame emission spectra for a low (J'=6.5), medium (J'=19.5) and high (J'=37.5) rotational number show little thermalisation due to the predominance of quenching in these collisional environments. Rotational distributions tend to remain peaked about the pumped level. Only for the low-J case the distributions appear to be thermal but at a temperature circa 280K, very well below typical flame thermodynamic temperatures. Emission spectra from a CH_4/air appear more thermalized than spectra from the CH_4/O_2 and H_2/O_2 flames in agreement with excited state lifetime estimates using quenching and flame model data. The flow cell data for N_2 and CO_2 shows that N_2 is efficient in RET with an overall thermalisation cross section of 10Å^2 for J'=6.5 and 2Å^2 for J'=19.5 resulting in thermalized emission spectra for both pumped lines. CO_2 is far more efficient at quenching and the rotational distributions observed via emission remain 'locked' far from thermalisation. In both flame and flow cell experiments the extent of thermalisation seems to decrease with increasing rotational number.

Acknowledgements.

Table of Contents

4.5.2. Diagnostic considerations.

Preface.

The dream of any chemist is to provide an accurate description of how a chemical reaction proceeds from reactants to products. By combining experiment and theory it is possible to postulate, in principle, the mechanism of a chemical process, be it an elementary decomposition reaction or a complicated biochemical pathway. Physical observables such as the identity and concentration of reactants, intermediates and products, temperature or pressure are essential pieces of information available only via direct observation and measurement. From the simplest to the most complicated processes one is compelled to gather as much information as possible so as to develop a picture consistent with empirical data and theory. In addition, new experimental input provides in many cases a stringent test to currently accepted physical models of chemical reactions; any discrepancies between experiment and model are used to improve the predictive capabilities of the latter.

The gas phase is the simplest medium for the study of chemical reactions. As of today, there is no other phase of matter understood in so much detail. Simplicity, however, does not imply a lack of relevance. Gas phase chemistry has proven to be of extreme importance not only from a purely scholarly perspective but also from a more general one. For example, understanding of gas phase atmospheric chemistry, including phenomena such as ozone depletion or pollution, are essential for responsible and intelligent environmental policy-making. Questions such as what pollutants are most dangerous or what their effects are in the short and long term can only be answered through an exhaustive study of the chemistry governing the composition and dynamics of the atmosphere. One could even be tempted to say that our future in this planet largely depends on a firm understanding of human effects in this 'large-scale beaker'.

Scientists interested in the study of gas phase chemistry have heavily relied on the development of new technologies for reliable monitoring of chemical species, measurement of their concentrations, etc. In the last twenty years, lasers have been moved to the avant-garde of gas phase chemical research and, as illustrated in section 1.3, laser

techniques such as laser-induced fluorescence (LIF) have been very useful in the field, from the study of very elementary chemistry such as bond-breaking to the elucidation of the complex set of reactions governing the chemistry of combustion.

Laser diagnostics relies heavily on the fundamentals of molecular structure and spectroscopy. With the advent of wave mechanics and the subsequent revolution in atomic and molecular physics, the framework required for reliable monitoring of chemical species has become increasingly available to the non-physicist. Sections 1.1 and 1.2 outline the basic foundations of molecular structure and spectroscopy with special focus on diatomic molecules. Nitric oxide, the molecule of interest to this work, has been used as an illustrative example of the principles briefly introduced in these sections. The theoretical and experimental spectroscopic data-base for diatomics of intrinsic chemical importance is quite extensive today allowing its use for proper identification and monitoring of these species in a host of different gas phase reactive environments. Nevertheless, new research frontiers in this area are far from being exhausted and there are still important gaps that have not been filled yet. As the next few paragraphs will reveal, this paper is an attempt to extend the present experimental data-base available for nitric oxide, a popular target in the study of gaseous chemical processes.

With LIF and other related techniques routinely used in this field, one is able to correlate the emitted radiation (fluorescence) from an excited atom or molecule to important physical observables of interest to the chemist, i.e. species identity, concentration, internal energy distribution, etc. As an analytical technique there are, however, certain prerequisites that need to be met. In LIF the crucial quantity is the quantum yield, introduced in section 1.3.1.2. Roughly speaking the quantum yield provides the experimentalist with a correction factor connecting emission intensity to state population. It accounts for losses in emission intensity due to inelastic, i.e. non--internal-energy conserving, collisions in the probed medium. Knowledge of this correction factor is, from a strictly practical viewpoint, very important to those interested in the use of laser diagnostics, and more specifically LIF, in the study of gas phase chemistry.

In addition, the study of inelastic collisional processes has a more fundamental relevance (see section 1.3.1.3). A microscopic understanding of any transport and/or

reactive process necessarily involves the study of collisions between atoms and molecules as well as how those collisions transfer energy in its various forms (kinetic, vibrational, rotational, electronic). A chemical reaction is ultimately driven by collisions which are able to modify the internal energy distribution and ultimately lead to the breakage and formation of chemical bonds. Therefore, understanding of the physical mechanisms behind energy transfer is of prime importance if we ever try to develop an accurate picture of any chemical process.

Section 2 presents in detail the spectroscopic and collisional data-base available at present for nitric oxide. The aim of this work has been to extend the body of experimental information available about a specific type of inelastic collisional process: rotational energy transfer. As section 2 shows, extensive work has been performed already on other types of energy transfer such as quenching while there remain important gaps in both vibrational and rotational energy transfer.

As explained above, the aims of the project were twofold, both looking at the application of laser diagnostics to chemistry as well as attempting to understand better the dynamics of inelastic collisions leading to rotational energy transfer in electronically-excited nitric oxide. Section 3 contains a description of the experiments as well as the results. In these experiments, it was possible to evaluate the importance of this process in an environment suitable for laser diagnostics, a flame, and at the same time correlate the trends found in the flames to the results of experiments performed in the flow cell at room temperature and under more controlled conditions. Section 4 is devoted to the discussion of the scientific implications of this study. In particular, it was possible to obtain estimates of the importance of rotational energy transfer in flames and correlate this with the characteristics of the collisional media nitric oxide is subjected to. These findings have important dynamic and diagnostic consequences of their own right but also raise additional questions that can only be answered via more elaborate experiments along with an effort to find a suitable theoretical framework that can explain and predict rotational energy transfer satisfactorily. One just hopes that the work presented here will foster further investigation in this complex and challenging field of research.

1. Introduction.

1.1. The energy levels of a diatomic molecule.

Crudely speaking, a diatomic molecule is a pair of atoms, connected by a spring and with four energy modes: electronic, vibrational, rotational and translational. To a first approximation all these degrees of freedom are independent of each other, allowing one to separate the total wavefunction for the molecule into four distinct wavefunctions as shown in equation (1).

$$\Psi_{total} = \Psi_{elec}\Psi_{vib}\Psi_{rot}\Psi_{trans} \qquad (1)$$

This approximation allows one to solve the Schrödinger equation for each individual mode. For vibrations and rotations, this equation can be solved exactly for the case of a harmonic oscillator, rigid-rotator molecule. The energy eigenvalues are then given by expressions 2 and 3 [2]:

$$G(\upsilon) = \omega\,(\upsilon + \frac{1}{2}) \qquad (2)$$

$$F(J) = BJ(J+1) \qquad (3)$$

where $G(\upsilon)$ is the vibrational energy, ω is the harmonic constant and υ is the vibrational quantum number. $F(J)$ is the rotational energy, B the rotational constant and J the rotational quantum number. In reality, this simple model is not capable of reproducing the observed spectra of even the simplest molecules because different energy modes actually couple and modify the expected energy level structure. It is necessary to consider each coupling case and examine its consequences. For a more detailed discussion see [3] .

1.1.1. The coupling of vibration and rotation.

As a molecule vibrates, the internuclear separation and consequently the moment of inertia change. Thus the rotational constant B shown above for the case of a rigid-rotator depends on the vibrational level the molecule is occupying. It is possible to define a rotational constant B_υ averaged over all rotational levels within a particular vibrational level υ in order to account for this coupling.

Furthermore, as the frequency of rotation increases the diatom tends to stretch due to the action of the centrifugal force. The moment of inertia increases and consequently the rotational constant B decreases. The effects of centrifugal distortion are accounted by a second constant D_υ. The correction to second order of the rotational energy is shown below. The subscript υ denotes dependence on the vibrational quantum number:

$$F(J) = B_\upsilon J(J+1) - D_\upsilon J^2 (J+1)^2 + \ldots \qquad (4)$$

1.1.2. The coupling of vibration and electronic motion: anharmonicity.

The harmonic oscillator model assumes that the electronic potential curve is a perfect parabola, i.e. the potential energy is proportional to the square of the displacement. In reality, electronic potentials only behave in such a way in the limit of zero displacement from the equilibrium position. The second order correction to the expression for G(υ), the vibrational energy, uses the same series expansion as that seen for vibration-rotation coupling. The vibrational energy can be then written as:

$$G(\upsilon) = \omega_e (\upsilon + \frac{1}{2}) - \omega_e \chi_e (\upsilon + \frac{1}{2})^2 + \ldots \qquad (5)$$

The subscript 'e' denotes the dependence of those constants on the particular

electronic state. The vibration-dependent rotational constant B_υ and the centrifugal constant D_υ introduced above also depend on the electronic state and can be written as a truncated series expansion of the form shown below:

$$B_\upsilon = B_e - \alpha_e \, (\upsilon + \frac{1}{2}) \, + \, \beta_e \, (\upsilon + \frac{1}{2})^2$$
$$D_\upsilon = D_e \, + \, \beta_e \, (\upsilon + \frac{1}{2})$$

$$(6)$$

All molecular constants introduced in 1.1.1. and 1.1.2. are obtained by fitting spectroscopic data to a power series expansion of the form shown in equations 4 and 5. A variety of fitting procedures have been devised for this purpose and the reader is referred to [6] where they are described in detail.

1.1.3. The coupling of electronic angular momentum and nuclear rotation [5].

Electronic-rotation coupling has profound effects on the appearance of spectra of diatomic molecules. So far the interaction of both the orbital and spin angular momenta of the electrons with the rotational angular momentum of the nuclei has been neglected. There are a total of five limiting cases for this type of coupling, Hund's cases (a) through (e) [55]. The diatomics that we will see in this paper can be all described satisfactorily by invoking only the first two cases.

Diatomic molecules have lost the spherical symmetry present in atoms but still retain axial symmetry about the internuclear axis. Electrons move around the nuclei in indeterminate directions with a total orbital angular momentum L. Λ, the projection of L onto the nuclear axis, is always a constant of the motion and can be used to characterize the electronic state of the molecule. Λ is said to be a 'good quantum number'. Apart from the orbital angular momentum, electrons poses an intrinsic spin angular momentum. The total spin angular momentum of the molecule is given by the letter S. The nuclear rotation quantum number can be any integer equal or greater than zero and indicates the rotational

state the molecule occupies.

In Hund's case (a), the electronic spin and orbital angular momenta are strongly coupled to the internuclear axis and the interaction between rotation and electronic motion is weak. A new quantum number Σ is defined as the projection of the total electronic spin onto the internuclear axis. Σ is combined with Λ to generate Ω, the total electronic angular momentum. The total angular momentum J is then the sum of Ω and N, the nuclear rotation quantum number. Figure 1 clarifies the coupling scheme in Hund's case (a).
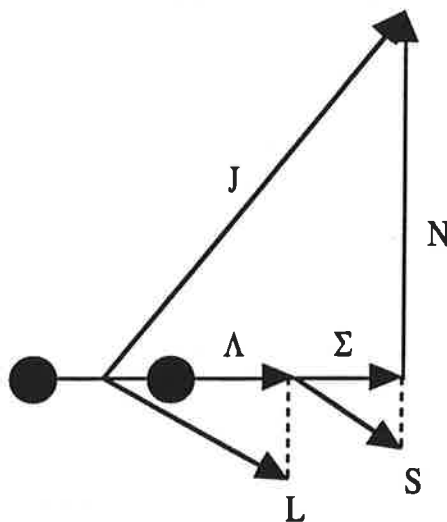
Fig. 1 Vector representation of Hund's case (a). Momentum vectors originate from the center of mass of the diatom. The projections of the electronic and spin angular momentum are first coupled to each other yielding Ω. Ω is then combined to the nuclear rotation quantum number to generate the total angular momentum of the molecule.

In Hund's case (b) the electronic spin is uncoupled from the internuclear axis (fig. 2). While Λ is still defined neither Σ nor Ω are. Λ and R, the nuclear rotation quantum number, are added together to yield N which then combines with S to give the total angular momentum J.
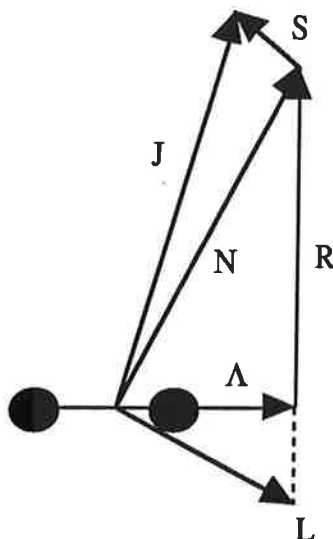
Fig. 2 Vector representation of Hund's case (b). Ω is no longer defined. Λ and the nuclear rotation quantum number combine first giving N. N then couples to S to give the total angular momentum.

1.1.4. Molecular electronic states: nitric oxide.

The convention used to designate molecular states in diatomic molecules uses a format of the type $^{(2S+1)}\Lambda_J^{parity}$. This term symbol contains all the information necessary to characterize the electronic state. S is the total spin and therefore 2S+1 is the spin degeneracy. Λ is the projection of the electronic orbital momentum and is written using the Greek letters Σ (Λ=0), Π (Λ=1), Δ (Λ=2), etc. J, the total angular momentum of the state apart from rotation, is the sum of Λ and S. For Σ molecular states (Λ=0) it is often convenient to include the parity, positive or negative, as a superscript. The parity of a molecular state denotes the behavior of the electronic wavefunction upon reflection through a plane containing the internuclear axis. It is + if the wavefunction does not change sign or - if it does. This is analogous to the symmetry properties of atoms where the symmetry of an atomic state is determined by the behavior of the wavefunction with

respect to an inversion through the center (gerade versus ungerade states).

It is worthwhile to apply at this point the concepts introduced so far to nitric oxide, the diatomic molecule of concern to this study. NO in its ground state is designated as X-$^2\Pi_{1/2,\ 3/2}$. The supercript '2' indicates that the state is twofold degenerate, that is, (2S+1) is equal to 2 or S, the total spin angular momentum is 1/2. NO is a stable free radical species. Its electronic configuration is $KK(\sigma_g 2s)^2(\sigma_u^* 2s)^2(\pi_u 2p)^4(\pi_g^* 2p)^1$, corresponding to an unpaired electron in the outermost antibonding molecular orbital. This lone electron, for example, explains its low ionization potential.
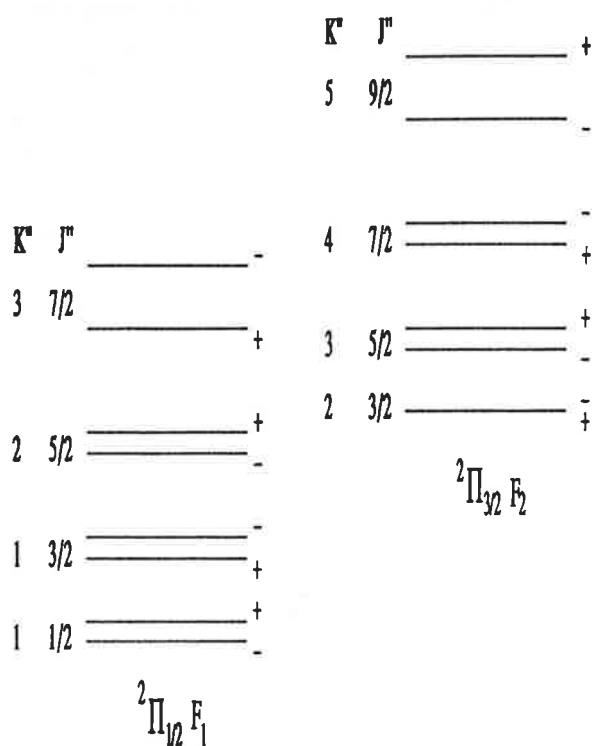
Fig. 3 Energy level diagram for the ground state of NO. Each state is labelled according to the total angular momentum and the properties of the rotational wavefunction.

Π shows that the orbital angular momentum is one. The existence of two different ground electronic states is due to the interaction of spin and orbital angular momentum, or spin-orbit coupling, yielding a total electronic angular momentum of Λ+S and Λ-S. The separation of these two spin-orbit states is circa 120cm^{-1} and both are populated at room

temperature (fig. 3). At low temperatures, however, all the ensemble population occupies the $^2\Pi_{1/2}$ state. As the temperature increases the fraction of molecules in the $^2\Pi_{3/2}$ increases and the ensemble starts behaving as a paramagnetic species. At high temperatures, significantly above 300K, NO has a bulk magnetic moment not present at low temperatures [3].

NO molecular states are intermediate cases between Hund's case (a) and (b). In the limit of small nuclear rotational numbers they can be regarded as case (a) but as the frequency of rotation increases they become case (b). For small rotational velocities, Ω is well-defined because both Λ and S are strongly coupled. As rotation increases the rotational velocity becomes comparable to the precessional velocity of S about Λ until the coupling between Λ and N becomes stronger than the coupling between Λ and S. At that point, Hund's case (b) describes better the ground state of nitric oxide.

Figure 3 shows the level structure of nitric oxide. Each rotational level is labelled with a '+' or a '-' in order to denote the symmetry properties of the rotational wavefunction. A rotational level is positive or negative depending on whether the total wavefunction remains unchanged or changes sign for a inversion at the origin. The symmetry properties of a rotational level are important in determining what transitions are allowed as it will be explained in section 1.2.

1.2. The interaction of a molecule with radiation.

Most conventional spectroscopies including the one used in this work take advantage of the interaction of the electric field of radiation with the dipole of the molecule. Electromagnetic fields can interact with higher multipoles of the molecule but such transitions are far weaker. For example, Raman spectroscopy takes advantage of the interaction of the molecular quadrupole with the radiation field. Despite being observed by Raman [50] in the early years of molecular spectroscopy, experiments using this technique were not possible until the appearance of lasers. Keeping ourselves within the domain of dipole-allowed transitions and spectroscopy, its conceptual framework can be properly understood by invoking a two-level system, introduced below.

UPPER LEVEL (f)

spontaneous
emission

absorption

stimulated
emission

rates:

absorption ρB_{if}

spontaneous emission A_{fi}

stimulated emission ρB_{fi}

LOWER LEVEL (i)
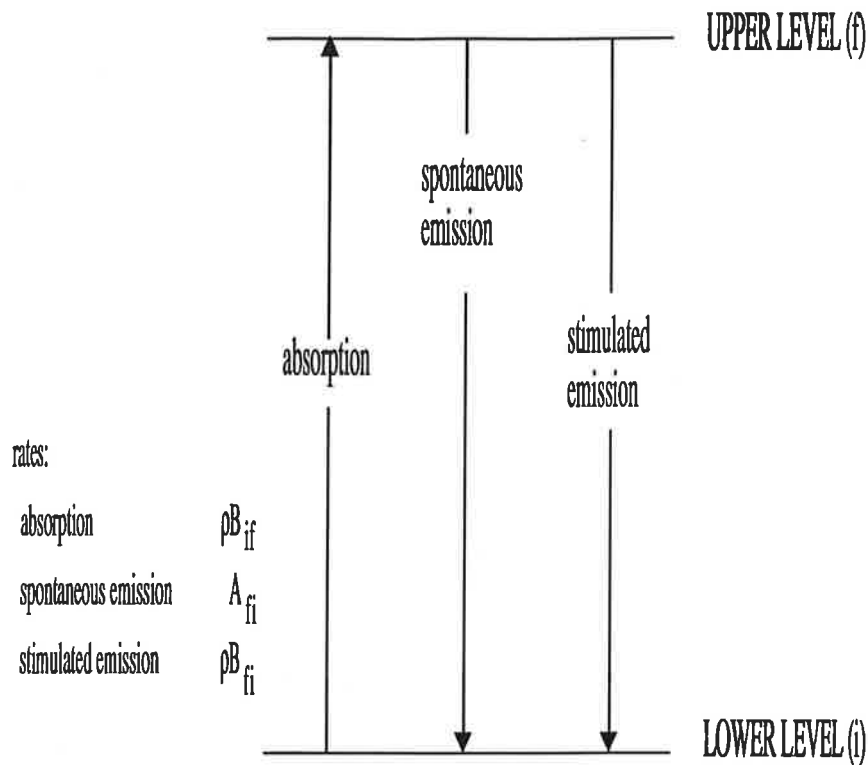
Fig. 4 Schematic diagram of the two-level system describing the three different types of interaction of an atom or molecule with electromagnetic radiation.

1.2.1. The two-level system [8,9].

The simplest case to consider is that of two energy levels and an electromagnetic field matching the energy gap between them. As figure 4 shows, three optical processes are possible: stimulated absorption, stimulated emission and spontaneous emission. Each process can be kinetically defined by a rate constant also called Einstein coefficient [8]. Stimulated processes require the presence of radiation and depend directly on the population of the initial level and the radiation density (i.e. they are second-order processes). Spontaneous emission, on the contrary, only depends on the population of the upper level (it is a first-order process).

Spontaneous and stimulated emission also differ in the way the photon is emitted. A stimulated emission photon has the same phase, direction and polarization as the incident photon. We say it is 'coherent' with the incident photon. In contrast, a photon emitted spontaneously is totally isotropic: its direction in space, phase, etc. are completely random. In order to understand conventional optical spectroscopy it is not necessary to consider stimulated emission because the population in the upper level will always be much smaller than that of the initial state and thus in the presence of radiation, absorption of photons will predominate over stimulated emission. Stimulated emission, for example, is important to understand laser action but is not relevant for the present discussion.

1.2.2. The Einstein coefficients.

In the two-level system explained above the Einstein coefficients were presented in a rather 'ad hoc' manner. In fact, there is an important connection between these coefficients and the quantum mechanical theory of molecular structure. The Einstein coefficients are proportional to the square of the transition dipole moment R_{if}, where i and f are the initial and final states (equations 7-9). The classical analogy of this quantum mechanical process is as follows: for a molecule to interact with an electromagnetic field and absorb or emit a photon it must possess, at least transiently, a dipole oscillating at such frequency. R_{if} is then a measure of the probability of a transition from i to f due to the interaction of a molecule, its dipole moment μ, and a radiation field.

$$R_{if}^2 = R_{x\,if}^2 + R_{y\,if}^2 + R_{z\,if}^2 \qquad (7)$$

$$R_{x\,if} = \int_{\tau} \psi_i \mu_x \psi_f \, d\tau \qquad (8)$$

$$\mu_x = \sum_i x_i q_i \; ; \; x\text{-comp. of the dipole vector.} \tag{9}$$

Equation 7 seven shows that the total transition dipole moment is the vector sum of x, y and z transition dipole moments. Each transition dipole moment can be calculated from equation 8, where ψ_i, ψ_f are the total wavefunctions for the initial and final states and μ_x is the x-component of the electric dipole moment (equation 9).

The Einstein coefficient for spontaneous emission between the final (f) and initial (i) levels separated by an energy gap of frequency ω is then given by:

$$A_{fi} = \frac{64\pi^4 \omega_{if}^3}{3h} R_{if}^2 \tag{10}$$

The coefficients of stimulated absorption and stimulated emission can be related to that of spontaneous emission if one considers equilibrium between a gas and a black body radiator. At equilibrium, the rate of transitions upward has to be equal to the rate downward, or according to the two-level system described before:

$$N_f(A_{fi} + \rho_{if} B_{fi}) = N_i(\rho_{if} B_{if}) \tag{11}$$

The radiation density ρ_{if} can be described by Plank's blackbody distribution while the gas obeys a Boltzmann distribution, i.e. level occupancy falls off exponentially with energy. Imposing these two restrictions in formula 11, the A coefficient may be related to B by the following formula:

$$B_{if} = B_{fi} = \frac{1}{(8\pi h \omega_{if}^3)} A_{fi} \tag{12}$$

Formula 12 shows an important relationship between the stimulated and

spontaneous emission coefficients. The stimulated emission coefficient is directly proportional to the spontaneous one but inversely proportional to the frequency of the transition. For example, at sufficiently high frequencies such as those typical of visible and UV radiation, B_{fi} is negligible compared to A_{fi} and only spontaneous emission needs to be considered in an analysis of the major radiative deactivation processes.

1.2.3. Transition probabilities in a diatomic molecule [7].

Assuming the internal modes of a diatomic molecule are independent, the transition moment for a given transition between single states can be represented in terms of separate electronic, vibrational and rotational contributions. For a transition between an initial state (e", v", J") to a final state (e', v', J'), the transition moment is factored out into the product of the electronic transition moment $R_{e''e'}$, the Franck-Condon factor $q_{v'',v'}$ and the rotational line strength $S_{J'',J'}$.

$$ R_{(e'',v'',J'')\,(e',v',J')}^{2} = R_{e'',e'}^{2}\ q_{v'',v'}\ S_{J'',J'} \qquad (13) $$

The Franck-Condon factors and rotational line strengths are normalized for the whole set of transitions from the initial level. In general:

$$ \sum_{v'} q_{v'',v'} = 1 \ ; \quad q_{v'',v'} = \left(\int_{\tau} \psi_{v''}\psi_{v'}\ d\tau \right)^{2} \qquad (14) $$

$$ \sum_{J'} S_{J'',J'} = (2J''+1) \qquad (15) $$

The Franck-Condon factors are evaluated by calculating the overlap integral between the initial and final vibrational wavefunctions. The rotational line strengths can

be regarded as normalization factors which give the relative strengths of rotational transitions between given vibrational levels. As in the case for the energy level structure of a diatomic, the assumption of mode independence is a poor one since the electronic transition moment is dependent on both the vibrational and rotational quantum numbers. Agreement with experiment is possible if we define the transition moment as the product of an electronic-vibrational transition probability, an independent transition probability for each vibrational level, times the rotational line strength.

1.2.4. Selection rules for dipole transitions.

It is tempting to think that all transitions matching the photon energy are allowed. However, photons have an intrinsic spin angular momentum and that limits all the plausible transitions to just a few. Selection rules are obtained by considering which transitions conserve angular momentum when a photon is emitted or absorbed. In the case of molecular dipole transitions this can be done by evaluating the transition dipole integral shown above and see whether it is zero. These rules, however, are not strict for two reasons: first, the molecular states under consideration may be intermediate cases between Hund's case (a) and (b); second, dipole-forbidden transitions may be allowed via the interaction of the radiation field with higher multipoles. Even in such cases, the dipole transitions are generally the most intense and readily observable.

The selection rules for dipole-allowed transitions are [3]:

(a) General case: applies to any atomic or molecular system.

  - Transitions between states of the same parity is forbidden.

  - $\Delta J = 0, \pm 1$ except for $J'' = 0 \rightarrow J' = 0$.

(b) Hund's case (a):

  - $\Delta J = 0$, forbidden when $\Omega' = \Omega'' = 0$

  - $\Delta \Lambda = 0, \pm 1$

  - $\Delta S = 0$

  - $\Delta \Sigma = 0$

(c) Hund's case (b):

- $\Delta\Lambda = 0, \pm 1$

- $\Delta S = 0$

- $\Delta N = 0, \pm 1$; $\Delta N = 0$ transitions are forbidden when $\Lambda' = \Lambda'' = 0$
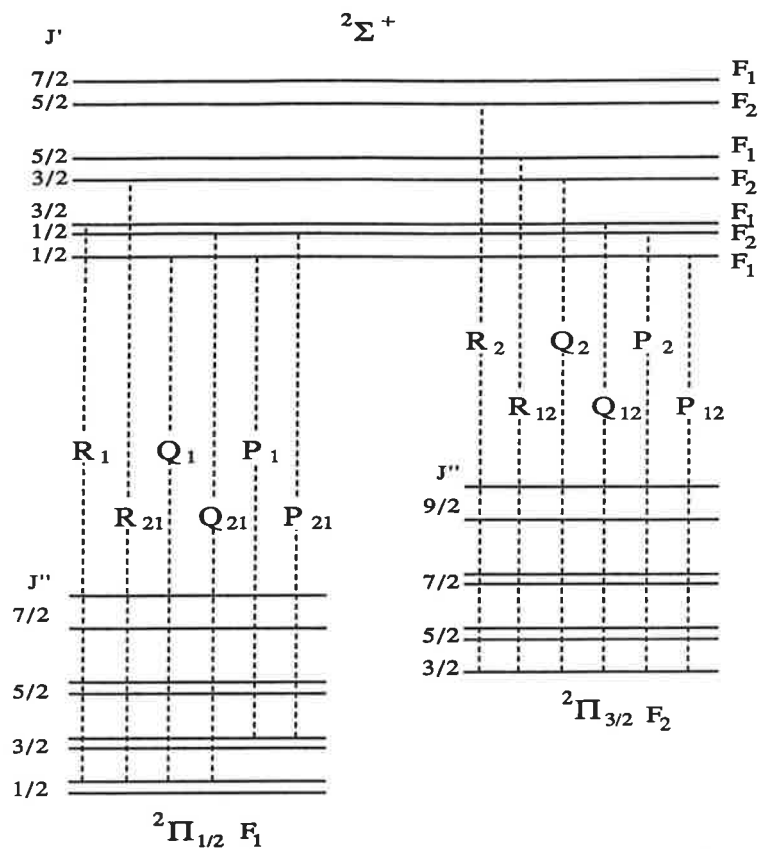

Fig. 5 Energy level diagram showing all twelve dipole-allowed upward transitions in a A-$^2\Sigma^+$-X-$^2\Pi$ system.

1.2.5. A-$^2\Sigma^+$ ← X-$^2\Pi$ transitions in nitric oxide [3].

The dipole selection rules presented in the previous section will be used to explain the spectroscopy of the (0,0) band of the A-$^2\Sigma^+$ ← X-$^2\Pi$ transition in nitric oxide near 226

nm. The diagram in figure 5 shows the lower and upper levels along with all possible dipole-allowed transitions. There are a total of twelve different branches given the spin-orbit splitting of both states. However, the splitting of the A-$^2\Sigma^+$ state is so small that it is not seen but at high resolution.

The nomenclature used for designating transitions varies in the literature. We have chosen that given by Deézsi [56] where lines are designated P, Q, R depending on whether the transition involves a -1, 0 or +1 change in total angular momentum respectively. Subscripts are used to denote the final and initial spin-orbit states and the total angular momentum of the lower state is given in parenthesis. For example $P_{22}(7.5)$ indicates that the transition originates from J"=7.5, goes to J'=6.5 (ΔJ=-1) and there is no change in spin orbit state; the transition starts in the F_2 spin orbit state of the lower level and ends in the F_2 spin orbit state of the upper electronic state.

1.3. Laser spectroscopy.

The word 'laser' is the acronym for 'Light Amplification by Stimulated Emission of Radiation'. Stimulated emission is attained by using very intense sources of radiation (i.e. a discharge) capable of generating a population inversion, i.e. a large portion of the molecules are excited and subsequently radiate. For our purposes, a laser is an intense, controllable, tunable, monochromatic and coherent source of radiation.

All these capabilities have been exploited intensively since the invention of the laser in the early sixties [13]. Before the laser era, for example, spectroscopists were rather limited in their experiments due to the lack of suitable sources of light that made very difficult the design of systematic quantum-resolved experiments. The boom of the field of molecular reaction dynamics during the 1960s and 1970s is a clear illustration of the impact lasers had in the experimental physical sciences. For the first time, the energy partitioning of reactants and products from elementary chemical reactions could be measured providing a means of directly looking at their mechanism [15]. More recently, femtosecond-pulsed lasers have been used to probe the for-so-long postulated transition state of a chemical reaction [16-18] and to study the relaxation dynamics of condensed

systems such as simple liquids, polymers, liquid crystals or supercritical fluids [19-24].

Lasers have not been restricted to highly specialized areas of science. An important feature we have not mentioned yet is their non-intrusive and non-disturbing character which makes them ideal probes of sensitive and/or hostile environments. For example, the technique of laser-induced fluorescence, has become standard in the study of flames [25], plasmas [26-30], etc .

An exhaustive classification of all the laser techniques in use today is beyond the scope of this brief introduction. For our purposes it is convenient to split up the laser world into two parts: linear and non-linear techniques [58]. This classification is based on the type of interaction of the laser with the probed atom or molecule. Linear spectroscopies like laser-induced fluorescence are generally based on a single-quantum interaction of the system with the radiation field and the signal observed is directly proportional to, among other things, laser intensity. Non-linear spectroscopies follow a more complicated relationship between the laser intensity and the signal observed and the specifics of such relationship vary from technique to technique [59].

Laser-induced fluorescence was one of the first laser spectroscopic techniques to be developed. In the 1970s and early 1980s most of the theory underlying this technique was mature allowing its use in both very elaborate experiments [10-12] as well as in problems of more direct practical relevance such as combustion [32]. Non-linear spectroscopy has remained behind laser-induced fluorescence and its use has been held back by the need to accumulate a body of information analogous to the laser-induced fluorescence data-base. However, many features of novel non-linear spectroscopic techniques predict a promising future and it is very possible that one day they will occupy the place laser-induced fluorescence has had for years. An example of this trend is REMPI (**R**esonance-**E**nhanced **M**ulti**P**hoton **I**onization), widely used in the study of reaction dynamics [35-37], and four-wave mixing techniques [38-41], which recently have started to compete with more conventional techniques in the study of hostile environments.

1.3.1. Laser-induced fluorescence (LIF).

The basic modus operandi of LIF is not difficult to grasp: a laser is tuned so that it matches the transition between two energy states in an atom or a molecule and then the emission or fluorescence from the excited state is detected by conventional means, e.g.. a photomultiplier tube. It is then possible to probe individual electronic-vibration-rotational states and thus obtain quantum-resolved information of the system under study [42,43].
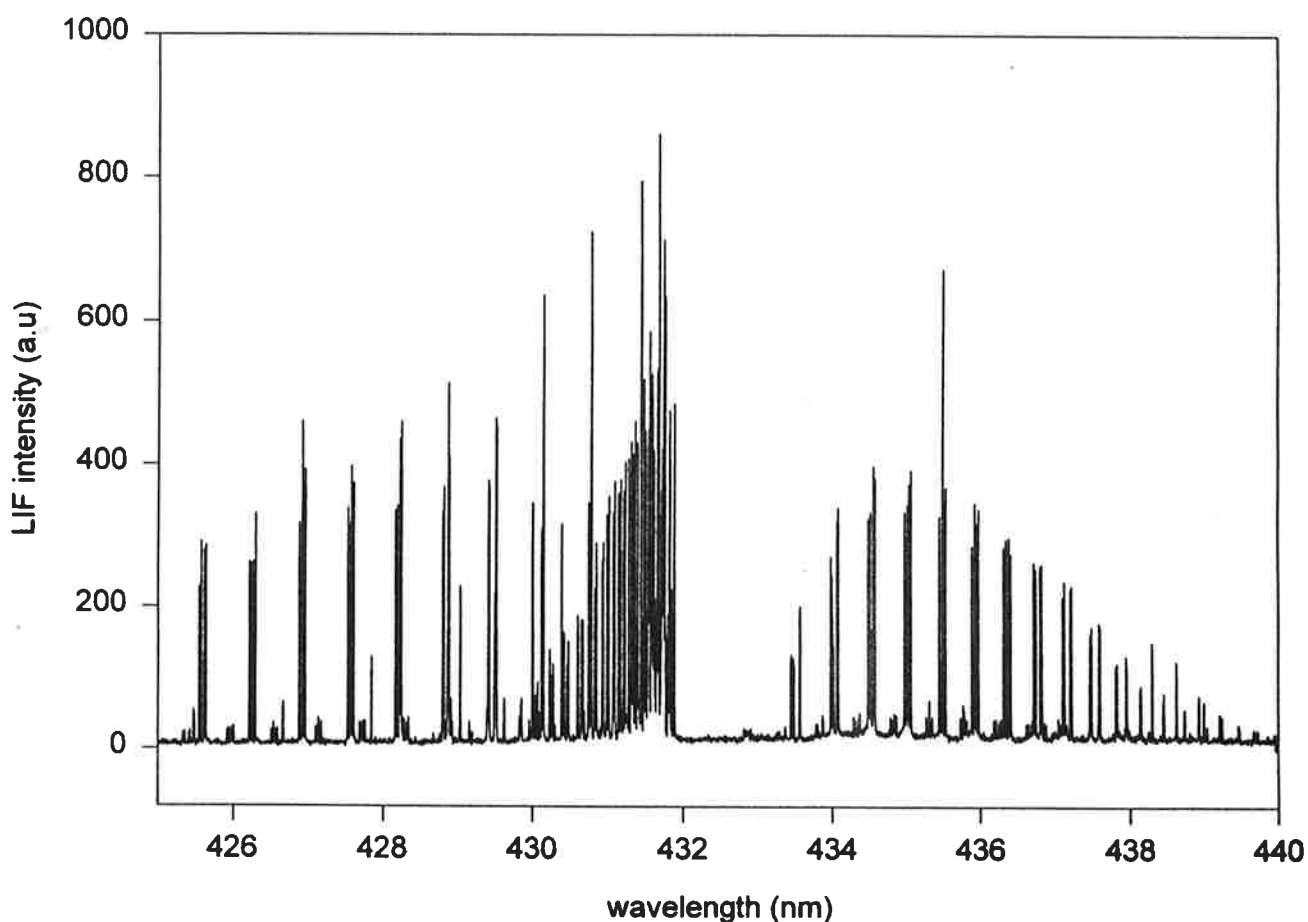

Fig. 6 Excitation scan of the (0,0) A-$^2\Sigma^+$-X-$^2\Pi$ band in the CH radical taken in a 40 torr propane-air flame. Each line corresponds to a transition to an individual rotational level of the excited state.

1.3.1.1. General Features.

LIF can be used to look at the ground or the excited state of a dipole-allowed transition. In the former case, a laser is tuned to a particular upward rovibronic transition and then the total fluorescence from the excited state detected (wide bandpass detection). By scanning the laser wavelength over a region the molecule is known to absorb it is possible to measure a background-free, rotationally-resolved absorption spectrum, a very difficult task to achieve by conventional absorption spectroscopy. Figure 6 shows an excitation scan of the (0,0) band of the A-$^2\Sigma^+ \leftarrow X$-$^2\Pi$ system of CH, an important combustion radical intermediate [44]. Each individual line corresponds to a single transition between rotational levels of the zeroth ground and excited vibrational levels. As it will be shown in 1.3.2 an excitation scan provides very useful information not only about the probed molecule (i.e. its relative concentration in the medium) but also about the environment conditions (i.e. temperature).

If instead of the lower state one is interested in studying the excited state the mode of operation is changed slightly. This time the laser is positioned at a particular upward transition and then the intensity of fluorescence is monitored as a function of detector wavelength (i.e. use of a monochromator). Rotational resolution is possible by using narrow-bandpass detection, that is, allowing a very narrow wavelength range about the bandpass center to be detected at a time. The resulting fluorescence spectrum can be related back to the population distribution of the excited state and provides a very convenient way of studying relaxation processes that take place after laser pumping. The experiments described in the third part of this paper use this approach to study the relaxation of the excited state due to collision-induced rotational transitions in the A-$^2\Sigma^+$ state of nitric oxide. The relevance of this type of study will be apparent in the next section where the concept of the quantum yield is introduced.

1.3.1.2. Analysis of LIF signals. The concept of the quantum yield.

Consider again the two-level system introduced in section 1.2.1. Molecules are

taken from the lower to the upper state via a dipole-type interaction. Once they are in the upper state, they relax back to the ground state via stimulated and spontaneous emission. Neglecting stimulated emission, the total fluorescence intensity can be written [45]:

$$F = KAN_f \qquad (16)$$

where F is the total fluorescence, N_f is the total population in the excited state and A accounts for the strength of the particular transition involved (it includes the electronic, vibrational and rotational probabilities). K is a geometry factor accounting for the solid angle of total fluorescence collected and the detector efficiency.

The situation described by equation 16 does not take into account the loss processes due to non-radiative transitions that take place in an ensemble of molecules. The expression shown in equation 16 for the fluorescence intensity is correct only in the case where there is an isolated molecule interacting with the electromagnetic field. In realistic systems this is far from being the case. Excited molecules are non-radiatively deactivated and the amount of fluorescence observed decreases. There are four main non-radiative pathways: electronic energy transfer out of the electronic excited state (quenching), vibrational energy transfer to other vibrational levels of the excited state (VET), rotational energy transfer to nearby rotational energy levels within the same vibrational level (RET) and predissociation.

Quenching, VET and RET are caused by inelastic collisions of the excited molecules with the surrounding environment. Therefore, their rates depend on both the concentration of excited state molecule and the concentrations of other species in the medium, i.e. kinetically speaking, they are second-order processes. Predissociation, of little relevance here, involves the dissociation of the molecule into fragments due to curve crossing of the excited state with nearby energy states corresponding to the molecular fragments. It is an important process when looking at transitions near the dissociation limit or when there is important mixing of the excited state with nearby states. As opposed to quenching, VET or RET, predissociation is a first-order process that only

-27-

depends on the concentration of the excited state population.

Proper account of these deactivation pathways leads us to the concept of the quantum yield Φ. Φ gives the fraction of the total fluorescence from the level initially excited. It is the ratio of the radiative emission rate (A_{fi}) and the sum of all deactivation pathways including A_{fi}. D denotes the contribution of all those processes apart from spontaneous emission that depopulate the excited level. It is written:

$$\Phi = \frac{A_{fi}}{(A_{fi}+D)} \tag{17}$$

Then the fluorescence observed can be written as:

$$F = \Phi \, KAN_f \tag{18}$$

From a knowledge of F, K, N_f and Φ it is possible to infer the population of the excited state and subsequently that of the ground state if the absorption probability is known. One of the most difficult tasks is to determine the quantum yield. It requires a knowledge of all temperature, species and state dependent rate constants responsible for each and every deactivation process as well as the concentration of each species present in the system. Determination of these rate constants is therefore of great concern to those interested in using LIF and other related techniques for quantitative measurements.

1.3.1.3. Collisional effects: electronic, vibrational and rotational energy transfer [46].

As it was pointed out in the previous section, quantitative application of LIF is quite limited unless one can determine the quantum yield. Each collisional deactivation pathway can be described by a phenomenological rate constant. For inelastic collisions,

the rate of removal is also dependent on the concentration of the collider and the temperature. The quantum yield can then be written as:

$$\Phi = \frac{A_{fi}}{\left(A_{fi} + \sum_i Q_i \left(k_{Q,i} + k_{VET,i} + k_{RET,i}\right)\right)} \qquad (19)$$

where k_q, k_{vet} and k_{ret} are all the species-specific, temperature-dependent rate constants and Q_i is the concentration of each collider in the medium. Quenching, VET and RET are described by the equations and corresponding rate laws shown below.

$$quenching: NO_{(e',v',J')} + Q \rightarrow NO_{(e'',v,J)}$$
$$rate: k_q [NO_{(e',v',J')}] [Q] \qquad (20)$$

$$VET(v_a' \rightarrow v_b') : NO_{(e',v_a',J')} + Q \rightarrow NO_{(e',v_b',J)}$$
$$rate: k_{VET} [NO_{(e',v_a',J')}] [Q] \qquad (21)$$

$$RET(J_a' \rightarrow J_b') : NO_{(e',v',J_a')} + Q \rightarrow NO_{(e',v',J_b')}$$
$$rate: k_{RET} [NO_{(e',v',J_a')}] [Q] \qquad (22)$$
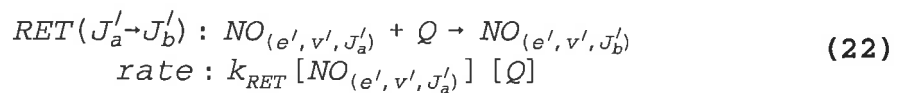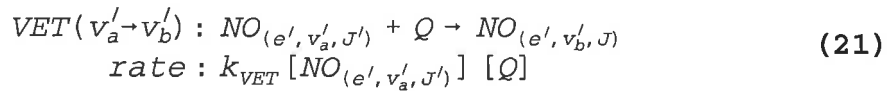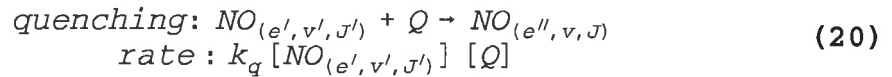
Theoretical investigation of these processes is still immature due to both a lack of sufficient experimental data and the complexity of the intermolecular forces taking place in the collision event. Calculation of a rate constant describing a collision event, be it reactive or not, requires a precise knowledge of the potential energy surface governing the process. This is a formidable computational task even for the best known systems [52].

Parallel to the theoretical interest behind the study of collisions, knowledge of these rate constants is essential if we are to use laser-induced fluorescence as an accurate diagnostic tool. Rate constants are generally obtained not from direct use of theory but from experiment. Two conceptual approaches are possible: time-resolved and steady-state experiments [53]. Quenching, VET or RET rates can only be determined if we can in some way measure the population distributions of the probed state as a function of time. In a generic laser experiment, a single rotational level in the excited state is populated and then allowed to relax. The simplest scheme is then to obtain time-resolved spectra at different times after excitation (i.e. electronically delaying the detection with respect to laser excitation) and from them derive the population distribution as a function of delay time. This time-resolved procedure can be difficult to implement experimentally due to the short time scales we are considering (10^{-6}-10^{-9} seconds). Alternatively, one measures a sequence of emission spectra at different collider pressures. This is known as the Stern-Volmer procedure [54]. The following general example illustrates how this is done.

Consider quenching of nitric oxide. Absorption, emission and quenching occur all the same time as described by equations 23, 24 and 25. Vibrational and rotational energy transfer are not considered in this case since we are only interested in measuring an overall quenching rate for a given electronic state, i.e. experimentally this is accomplished by measuring the total fluorescence from the excited state.

$$absorption: NO_{(e'',v'',J'')} + h\upsilon \rightarrow NO_{(e',v',J')}$$
$$rate: k_{abs} [NO_{(e'',v'',J'')}] [h\upsilon] \qquad (23)$$

$$emission: NO_{(e',v',J')} \rightarrow NO_{(e'',v,J)} + h\upsilon$$
$$rate: k_{em} [NO_{(e',v',J')}] \qquad (24)$$

$$quenching: NO_{(e',v',J')} + Q \rightarrow NO_{(e'',v,J)}$$
$$rate: k_q [NO_{(e',v',J')}] [Q] \qquad (25)$$

-30-
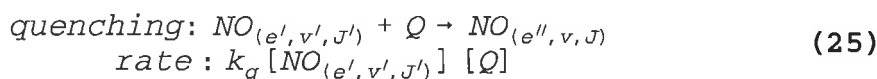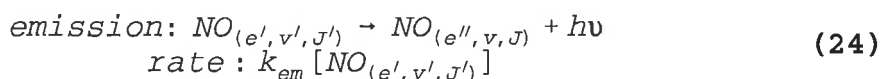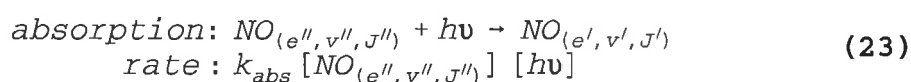
The quantum yields without and with the collider are:

$$\phi_0 = \frac{k_{em}}{k_{em}} = 1 \qquad (26)$$

$$\phi_q = \frac{k_{em}}{k_{em} + k_q [Q]} \qquad (27)$$

The self-quenching process has been neglected in this analysis by making the quantum yield without collider equal to one. This holds at very small concentrations of the fluorescing species in comparison with the concentration of collider. The ratio of quantum yields then gives:

$$\frac{\phi_o}{\phi_q} = 1 + (\frac{k_q}{k_{em}}) [Q] \qquad (28)$$

A plot of the ratio of the quantum yields or LIF intensities with and without the collider versus quencher concentration or pressure should be linear with a slope equal to the ratio of the quenching and the radiative rate constant.

Rate constants for quenching, VET or RET are generally reported as collision cross sections expressed in area units (usually $Å^2$). Cross sections can be interpreted as a measure of how close two molecules have to be for the process to occur and are directly proportional to the likelihood of the process. Large cross sections, for example, indicate that the process is very probable, i.e. fast, and governed by attractive, long-range forces. Small cross sections, on the contrary, are indicative of a slow, short-range process.

-31-

From collision theory [2], the rate constant k and the cross section σ are related by:

$$k = \sigma \; v_{pair} \qquad (29)$$

where v_{pair} is the relative velocity of the colliding pair of particles and is given by:

$$v_{pair} = (\frac{8KT}{\pi \, \mu_{pair}})^{1/2} \qquad (30)$$

where T is the temperature and μ_{pair} the reduced mass of the collision pair.

1.3.2 Applications of LIF: probing combustion chemistry in a low-pressure propane-air flame.

Lasers have found wide applicability in atmospheric [31] and flame chemistry [25] because of their non-intrusive character as well as their high degree of sensitivity and species selectivity. All examples shown in this section are part of a set of experiments performed in a propane-air flame [47] prior to the RET measurements that make up the main body of this paper.

LIF is used in flame studies in order to investigate combustion chemistry. Two pieces of information are essential to reach some understanding of the flame chemistry: the temperature profile and the concentration profiles of different atomic and molecular species. A profile is a plot of a variable of interest (i.e. species concentration) versus the distance over the burner surface. At the surface, the reactants mix and start reacting as they flow through the flame. At sufficiently large distances away from the burner all chemistry has already occurred and only the final products of combustion are present. Thus, distance from the burner surface provides a means of looking at the temporal evolution of the flame chemistry. In general, this body of experimental data is then

-32-

contrasted against a computer model in order to test our *a priori* understanding of the flame chemistry and modify it accordingly. Temperatures are generally used as input to the computer model. Many chemical reaction rates have an exponential temperature dependence requiring a knowledge of the temperature to use the correct reaction rate constants in the computer model. As it will be shown, they are also necessary to convert LIF signals to species concentrations.
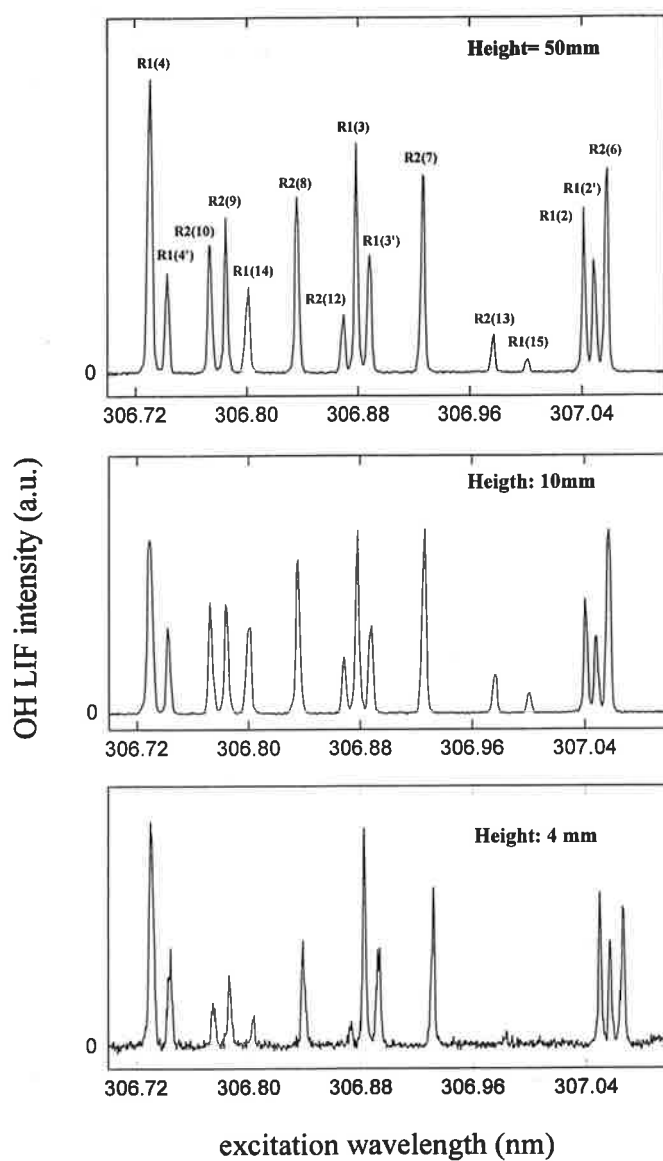
Figs. 7-9 Excitation scans of the A-$^2\Sigma^+$-X-$^2\Pi$ system in OH taken at different heights in a 40 torr propane-air flame.

Temperature in a flame is obtained by choosing a molecule with a wide envelope of rotational lines like for example OH. The OH radical has played a vital role in the development of laser diagnostics. It is an important intermediate in nearly all flames involving some form of hydrogen and oxygen. It is also known to be of crucial importance in the chemistry of the Earth's atmosphere. OH atmospheric reactions are responsible for the removal of trace species (CO, H_2, hydrocarbons, halocarbons) and directly affect the NO/NO_2 balance [57]. Its presence is generally used to signify the occurrence of oxidation reactions. It has been the species used for testing new diagnostic methods and generally the first molecule to search for when studying a new system. For temperature measurements it is generally the molecule of choice if present at sufficiently high levels because it has been well-studied and has well-resolved spectral features. Other molecules besides OH have been used for thermometry. Examples are CN, NH, CH [48] and NO. Figures 7-9 show three different excitation scans of the $A\text{-}^2\Sigma^+ \leftarrow X\text{-}^2\Pi$ system of OH at three different heights over the burner surface.

An LIF excitation scan provides a direct relationship between the intensity of the lines and the relative population of each individual rotational level in the ground state as shown by equation 31.

$$I_{TOTAL\ LIF} \ \alpha \ N_{J''} \ S_{J''} \qquad\qquad (31)$$

Furthermore, if the sample is at equilibrium the population distribution of the ground state obeys a Boltzmann distribution characterized by a rotational temperature T as shown below.

$$\frac{N_{J''}}{N_{total}} = \frac{(2J''+1)\ e^{\frac{(-hcBJ''(J''+1))}{kT}}}{Q_r} \qquad\qquad (32)$$

-34-
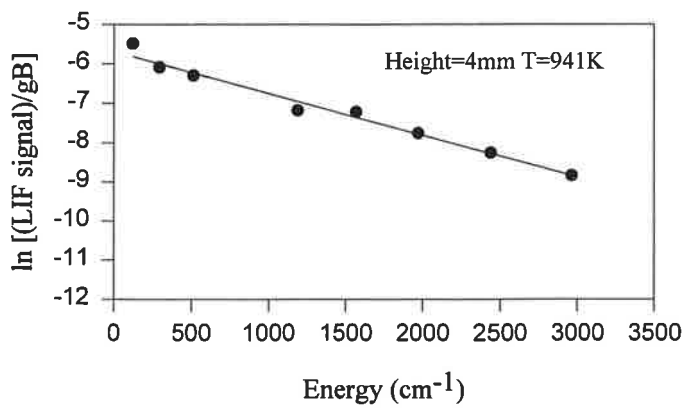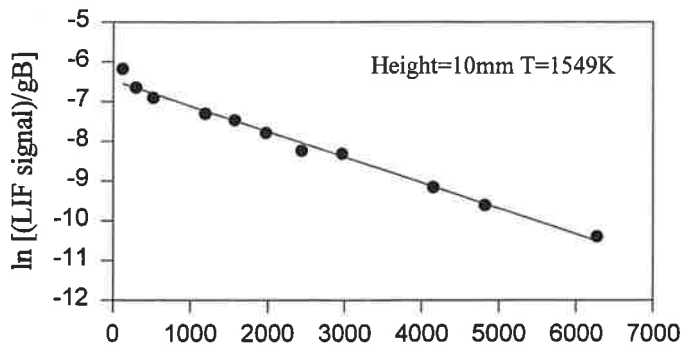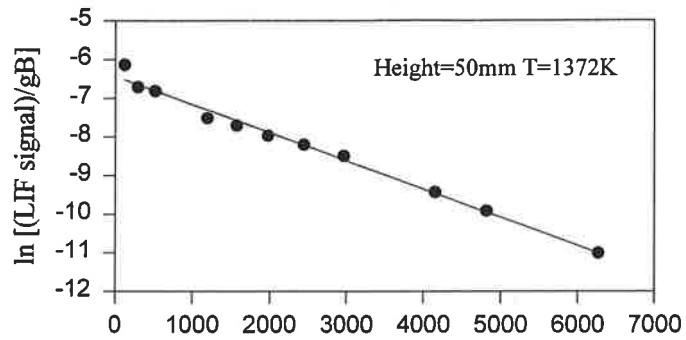
Figs. 10-12 Boltzmann plots of the OH excitation scans shown in figures 7-9. Linear behavior is expected for a rotational population at thermal equilibrium. Rotational temperatures are obtained from the slope of a linear fit to the data as explained in the text.

where B is the rotational constant and Q_r the rotational partition function. Combining equations 31 and 32 and removing the exponential dependence by taking the natural logarithm on each side one obtains the following linear relationship:

$$\ln\left(\frac{I_{TOTAL\,LIF}}{S_{J''}(2J''+1)}\right) = K - \frac{hcBJ''(J''+1)}{kT} \tag{33}$$

If the distribution is thermal, plotting the logarithm of the total intensity versus the energy of that particular level should yield a straight line with slope $-1/kT$. K is a constant including all those factors that do not change over the manifold of rotational levels, i.e. the total rotational partition function, detection efficiency, solid angle collection, etc. This is called a Boltzmann plot and three examples corresponding to the excitation scans in figures 7-9 are shown in figures 10 through 12. Special care must be taken experimentally for accurate temperature measurements. These precautions are:

(1) The LIF should be collected as soon as possible in order to avoid relaxation and non-radiative losses.

(2) Use of a wide detection bandpass to ensure that all the LIF is collected. Short bandpass collection will bias the LIF detection over certain pumped rotational lines and thus artificially affect the intensity distribution.

(3) Laser intensities should be below saturation (i.e. LIF should be a linear function of laser intensity). This restriction ensures a linear relationship between the fluorescence intensity and the relative population of the ground state rotational level pumped.

Figure 13 shows the temperature profile of a 40 torr, Mn-seeded propane-air flame [47]. Each point has been obtained from a temperature analysis of OH excitation scans. The rise in temperature occurs at the so-called flame front where most of the chemistry

occurs after reactants have had enough time to mix. Flame experiments are frequently performed under sub-atmospheric pressure conditions in order to expand the flame front, increasing the spatial resolution, and to reduce collision rates. Given a typical laser beam diameter of 0.5 mm it would not be possible to spatially isolate the flame front in a flame at atmospheric pressure due to the increased reaction velocity resulting in a narrower flame front. The flame front would occur very close to the burner surface, only allowing one to see the slow decrease in temperature with height typical of the burnt-gas region. Uncertainties in the measurements are generally in the order of 40K, sufficient accuracy to make quantitative comparisons with other systems and the computer model.
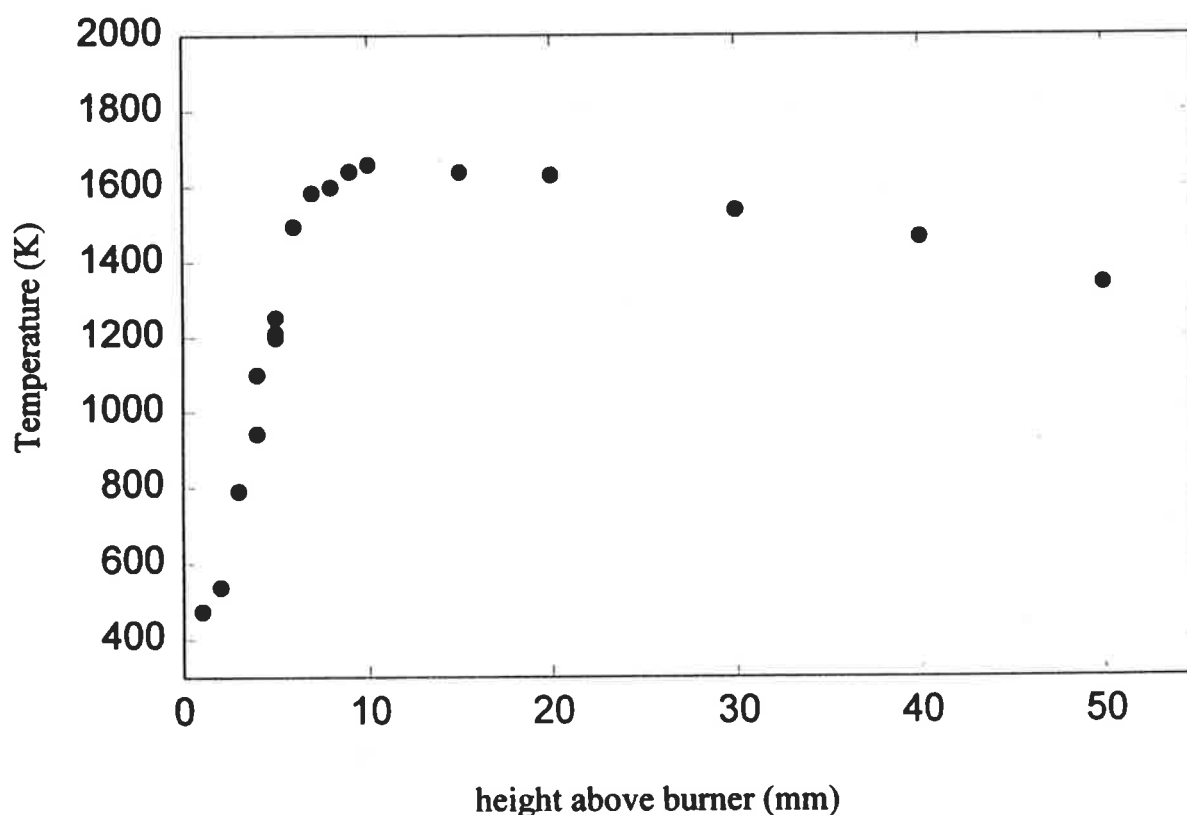
Fig. 13 Temperature profile of a 40 torr, propane-air flame derived from (0,0) A-$^2\Sigma^+$–X-$^2\Pi$ OH excitation scans. Typical temperature uncertainties are circa 40K, sufficient to obtain important chemical information about the flame.

Species profiles are measured in a similar way. This is the experimental data which is actually contrasted against the computer model that uses the measured temperature profile. In a species profile, one uses a transition with little temperature dependence, i.e. one that sits at the peak of the rotational distribution at normal flame temperatures. One then pumps this transition and selects a detection scheme such that no other atom or molecule is detected at the same time. Furthermore, with a laser beam diameter of 0.5 mm it is possible to obtain enough spatial resolution over the height range of interest, usually the first few millimeters over the burner. LIF intensities are then converted to relative concentrations using the measured temperature. Absolute measurements are usually performed by calibrating the experimental set-up with a known sample and then comparing the LIF signals with those obtained in the flame.
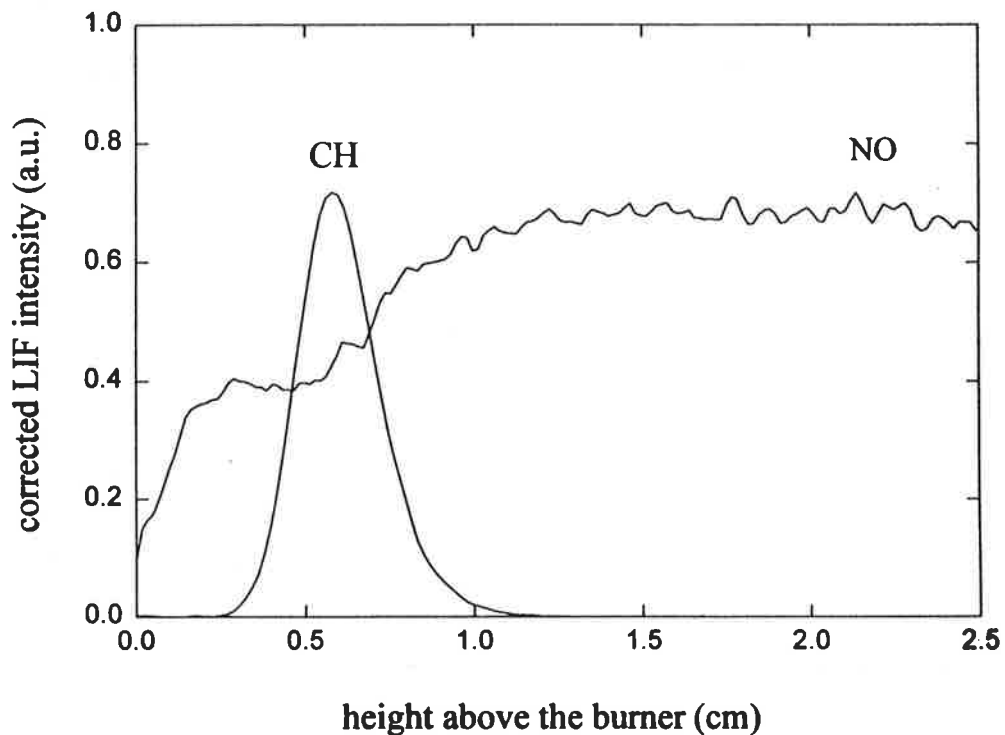
Fig. 14 NO and CH radicals profiles in a 40 torr propane air flame. CH is present in a very narrow range while NO persists all throughout the reaction zone and in the burnt-gas region. Early NO, prior to the appearance of CH, may be attributed to diffusion within the flame environment.

NO and CH profiles along the propane-air flame are shown in figure 14. Both species are present at very low concentrations. NO concentrations are in the part-per-million range and its absolute density can be determined by comparing the LIF signals from the flame with signals from a cold NO sample of known concentration. Other calibration techniques are possible. For example, in the case of the highly reactive CH radical, its concentration can be determined by comparing the fluorescence signals with those produced by Rayleigh scattering from N_2. Besides NO and CH, the work described in ref. 47 (appendix I) shows background-free profiles for OH, CO, O, H, Mn and MnO.

The role of CH radicals in the overall flame chemistry is still unknown due to the lack of reliable rate constant data at high temperatures. Given its high reactivity, however, it is used to mark the reaction zone [34].

In figure 14, the NO profile shows a continuous rise with height. Two chemical mechanisms are thought to be responsible for NO production in flames: a prompt mechanism at low flame temperatures (i.e. 800-900K) whose precursor is the CH radical and a thermal mechanism operative above 2000K. The two profiles shown here agree with the former mechanistic picture. Temperatures are never above 1700K and thus the thermal mechanism is ruled out. Furthermore, NO formation seems to be correlated with the presence of the CH radical. The NO concentration remains constant after all the CH has been consumed suggesting that prompt-NO formation is the only mechanism operative.

2. Statement of the problem: the nitric oxide data-base.

The energy level structure as well as the spectroscopy pertaining the A-$^2\Sigma^+$-X-$^2\Pi$ system of nitric oxide was explained in the previous section. In the introduction we also emphasized the importance of detailed knowledge of quenching, VET and RET of any species probed by LIF so as to make this technique as quantitative and accurate as possible.

Considerable advances have been made in the past two decades in the study of the spectroscopy and collisional processes in diatomics. A prime example is the OH radical, the most widely studied diatomic molecule. Other atomic and molecular species under the reach of LIF have not received the same amount of attention. This is the case of nitric oxide.

It is the purpose of this section to discuss the general relevance of nitric oxide as well as to present the current status of its spectroscopic and kinetic data-base so essential for the application of laser diagnostics.

2.1 Generalities.

Nitric oxide is an active molecule in various regions of the atmosphere [60,61]. In the stratosphere, it is produced by the oxidation of N_2O by $O(^1D)$. N_2O is mainly a product of microbial metabolism and is present at relatively high concentrations. Other sources are high altitude aircraft, nuclear explosions, volcanoes and lightning. In this region, NO and other NO_x species play an important role as catalysts in the destruction of ozone. This process is shown below:

$$NO + O_3 \rightarrow NO_2 + O_2$$
$$NO_2 + O \rightarrow NO + O_2$$
$$overall: O_3 + O_2 \rightarrow 2O_2 \qquad (34)$$
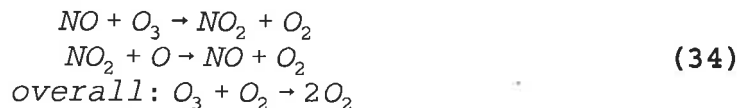
Surprisingly, nitric oxide plays an essential role in the production of ozone in the troposphere, an undesirable process due to the toxicity of ozone and its participation in pollution processes. The reactions leading to ozone production are shown below:

$$NO_2 + h\nu \rightarrow NO + O$$
$$O + O_2 + M \rightarrow O_3 + M$$
$$OH + CO \rightarrow H + CO_2$$
$$H + O_2 + M \rightarrow HO_2 + M \qquad (35)$$
$$HO_2 + NO \rightarrow OH + NO_2$$
$$overall: CO + 2O_2 + h\nu \rightarrow CO_2 + O_3$$
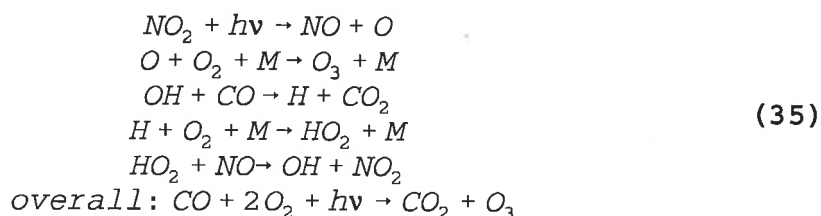
Sets of reactions like this one lead to the generation of the well-known 'photochemical smog', so typical of heavily populated or industrialized areas. The main NO_x source in these areas is engine combustion. NO is known to be produced in nearly all combustion environments containing nitrogen, including 'clean' fuels such as natural gas. Current flame research focuses on the elucidation of the different chemical mechanisms that lead to the formation of nitric oxide in combustion. As section 1.3.2 points out there are two main postulated mechanisms: thermal and prompt NO formation and which of them is operative depends on factors such as the flame temperature and the presence of radical intermediates such as CH. Ultimately, understanding of these mechanisms might allow us to reduce the NO levels that are currently unavoidable due to the generalized use of fossil fuels.

Parallel to flame research, there is also an increasing interest in probing the present NO levels in the atmosphere. Questions such as the anthropogenic effects of NO concentrations in the atmosphere are still open to debate.

LIF is definitely one of the favorite candidates to perform any gas-phase study on

this relevant species. Its success as a quantitative diagnostic probe, however, depends on a large body of experimental data on the spectroscopy, quenching, VET and RET of this molecule.

2.2. Spectroscopy of the A-$^2\Sigma^+$-X-$^2\Pi$ system.

The spectroscopy of the A-$^2\Sigma^+$-X-$^2\Pi$ system in NO was laid out before the laser era. In a historical paper dating from 1958, Deézsi [56] published an atlas of rotational transitions for the ultraviolet and visible bands of NO worked out during the 1940s by his predecessors Schimd and Gerô. The high quality of this work makes it even today an invaluable reference. Extensions to this stupendous body of data have proceeded until today. Most efforts have been focused on the refinement of the molecular constants of different electronic states [62,63,64,66], measurement and calculation of Hönl-London factors [65] and determination of emission rates of excited states [67,68].

2.3. Quenching.

Assher et al. [69] were the first to undertake an extensive and systematic study of quenching in the A, C and D Rydberg states for a large number of colliders. Before this work, quenching data was scattered in the literature in a rather spotty fashion. In this work, it was found that at room temperature colliders such as CO_2, NO, CCl_4, Cl_2 and NO_2 had large cross sections while N_2's was insignificantly small. In an attempt to rationalize these empirical findings they postulated a 'harpoon' mechanism involving the existence of an ion-pair intermediate complex and the crossing between ionic and potential energy curves. In this model, nitric oxide is the electron donor and the quencher molecule is the electron acceptor. The rate determining step of the energy transfer process is an electron jump from nitric oxide to the quencher leading to the formation of the ion-intermediate complex which upon separation yields ground state nitric oxide and quencher with large excess of energy associated with nuclear motion. According to this physical picture, the quenching cross section is given by πr_c^2 where r_c is the intermolecular distance

where the NO^+-Q^- surface cross the NO(A)-M surface. This model was later corroborated [70] by an extension of this study to a larger number of colliders.

The temperature dependence of NO quenching has only been investigated recently. These studies have been crucial in assessing both the reliability of the 'harpoon' mechanism as well as in providing new ways of understanding the nature of the intermolecular forces taking part in the process. Raiche et al. [72] studied the temperature dependence of the A and B states for N_2, O_2, NO and H_2O. It was found, in agreement with previous data, that quenching cross sections for all colliders but N_2 were generally large. However, only H_2O quenching of the B state seemed to have a clear dependence on temperature, in contradiction with the predictions of the harpoon model.

These discrepancies between experiment and model predictions have fostered further investigation. Temperature-dependent quenching has been recently continued by Drake et al. [74] in an extensive study including H_2O, CO_2, O_2, NO, N_2, CO, Ar, H_2 and C_2H_6 between 300K and 1750K. The experimental results allowed an empirical subdivision of quenchers in two groups. Strong quenchers, i.e. H_2O, CO_2, O_2 and NO, are molecules with positive electron affinities and quenching probably occurs via the formation of either a molecular or ionic collision complex. Weak quenchers, i.e. Ar, CO, N_2 and CH_4, possess negative electron affinities and quenching is thought to occur via a transfer into another low-lying NO electronic level and not from the A state directly. This extensive work is complemented by shock-wave experiments of N_2 quenching between 300K and 4500K recently carried out by J. W. Thoman et al. [73]. The harpoon model proved remarkably accurate in reproducing the temperature dependence of NO quenching by N_2, adding further evidence in support of this mechanism.

Despite the ongoing uncertainties regarding the physical explanation of the quenching mechanism, it has been possible to make use of the experimental cross sections and use them in the calculation of approximate quantum yields in environments of chemical interest. Heard et al. [71] found reasonable agreement between the measured quenching rates in a CH_4/air flame and those estimated from quenching cross sections and computed flame composition.

2.4. Vibrational energy transfer.

VET in the A-$^2\Sigma^+$ state has been studied at room temperature. Klemperer el al. [77] observed that VET by NO was more efficient than expected with cross sections circa 3Å^2. N_2, on the other hand, induced very little VET with a cross section at least two orders of magnitude below NO. VET mechanisms invoking resonant vibrational energy transfer [76] and widely accepted prior to this experiment had to be ruled out since both NO and N_2 have near-resonant vibrational energies. Gordon et al. [78] developed a model explaining VET in terms of electronic energy exchange governed by dipole-dipole forces between the two interacting molecules. These findings have been recently corroborated by Imago et al. at 298K [75] and by Thoman et al. at 1000K [73]. The temperature dependence of the VET cross sections follow the predictions laid out by the electronic energy exchange mechanism previously explained.

No further investigation of VET in the A-$^2\Sigma^+$ state has been performed to date. VET experiments are generally found as part of more extensive work focusing on electronic deactivation, i.e. see ref. 73.

2.5. Rotational energy transfer.

Rotational energy transfer in atomic and molecular species is of a more complicated nature than either quenching or VET. The relatively close spacing between energy levels generally requires an analysis of all state-to-state rate constants connecting rotational levels in order to develop a picture of the physical mechanism underlying this process. This is not the case for quenching, for example, where one collision takes the molecule from the excited to the ground state with no possibility of backward return to the original state via inelastic collisions. RET is therefore a complicated problem not only experimentally, i.e. design of carefully-tailored experiments, but also theoretically.

Collisional energy transfer rates for quenching, VET or RET [81] are ultimately related to the potential energy surface (PES) of interaction of two particles. Detailed PES have been calculated very recently for OH*-Ar, OH*-He [79] and CO*-Ar [80]. No

calculations of potential energy surfaces for NO A-$^2\Sigma^+$ are available at the moment even for collisions with noble gases. Furthermore, the state-of-the-art computational power is unable to perform accurate calculations of PES for diatomic-diatomic collisions. Given this limitation, the body of experimental data available on RET has been used to generate empirical and semi-empirical expressions that seem to fit experiment quite satisfactorily [82-84]. These empirical correlations, like the exponential-energy-gap (EGL), statistical-power-gap (SPG) or the energy-corrected-sudden-approximation (ECS), have been developed given the large number of quantum specific studies on dialkali-noble gas [85,86] and diatomic-diatomic collisions [87-89] performed in the last decade. In very general terms, these semi-empirical approaches correlate the likelyhood of rotational energy transfer to parameters such as energy level spacing, degeneracy factors, etc. Unfortunately, none of these studies touch those systems of interest to laser-diagnostics.

There are a number of old studies from more than two decades ago which mainly concentrate on the OH radical. The first of such studies was performed by T. Carrington [90] followed by Kaneko et al. [91] and Kley et al. [92]. These experiments gave the first measured estimate of the total relaxation rate in OH-A-$^2\Sigma^+$. For the very few rotational levels covered (K=13 and 20) a large probability of transfer out of the pumped rotational level compared to the overall deactivation rate was found. Dating from the same period there are a number of studies in other diatomics such as I_2 [93], CN [94], CH [95] and NO [76]. The nitric oxide rotational energy transfer studies in A-$^2\Sigma^+(\upsilon'=1)$, exciting a single rotational level (J'=12.5,13.5) revealed that for a large number of colliders including He, Ar, H_2, N_2, NO and CO_2 the emission spectra were not consistent with a mechanism involving only $\Delta J=1$ rotational transitions. Jumps of four and five rotational levels were necessary to account the experimental findings, a result in sharp contrast with previous theoretical considerations suggesting a propensity for $\Delta J=1$ transitions..

Investigations of RET in the OH radical were continued in the seventies by Lengel et al. [96] and permitted the calculation of the first state-to-state rotational energy transfer cross sections for N_2, H_2 and Ar. Immediately after these fundamental studies, RET started being investigated in more complex media such as flames [46, 97, 98].

The NO data-base lags far behind OH. Apart from Carrington's study [76]

pumping a single rotational level and deriving overall room-temperature relaxation rates for a number of colliders including NO and CO_2 there are very few experimental studies performed to date. Mallard et al. [99] have reported an approximate total rotational relaxation cross section of 70 Å^2 in a H_2/air/N_2O flame but this estimate was hampered by the lack of high-temperature quenching data at the time and the results relied heavily on extrapolations from previous RET studies, mainly on OH. Qingyu et al. [100] have studied very recently NO-NO RET at room temperature for three different rotational levels. The relaxation patterns varied with rotational level pumped. For N=7, the rotational quantum number most heavily populated at room temperature, relaxation was symmetrical with respect to the initially-pumped level. For levels above and below N=7, the distributions were largely asymmetric so as to approach the thermal population characteristic at room temperature.

2.6 Extending the data-base.

From the previous sections it is clear that the nitric oxide data-base is lacking both VET and RET data in comparison to quenching. Of special attention is the case of RET whose relevance in quantum yield determinations contrasts with the astonishing scarcity of experimental data available to date.

In section 3 we describe a set of experiments aimed at understanding rotational relaxation and energy transfer in the A-$^2\Sigma^+$ state of NO both at room temperature and in flames. It has not been possible to attain quantum-specific information about the individual, state-to-state RET cross sections. In spite of this limitation the data and results presented provide an appropriate starting point for further investigation.

3. Rotational energy transfer in A-$^2\Sigma^+$ NO in atmospheric flames and flow cells [111].

3.1 Description of the experiment.

3.1.1 Experimental set-up.

A schematic diagram of the experimental set-up is shown in figure 15. This arrangement was used for both the flame and flow cell experiments using a sintered-brass, water-cooled McKenna burner or a room-temperature flow cell in either case. In the flame experiments, nitric oxide was seeded into the premixed gases as pictured in figure 15.

An excimer laser (Lambda Physik EMG 100-201, XeCl) operating at a repetition rate of 20 Hz at 308 nm pumped a dye laser (Lambda Physik FC 2002) to generate laser radiation in the 450-460 nm range (Coumarin 2 4500, 1.5 g/l). At optimum operating conditions, the dye laser output had a power of 5 mJ/pulse.

A BBO (β-barium borate) crystal was used to double the fundamental harmonic to 226 nm, the wavelength necessary to excite $^2\Pi$ NO to the $^2\Sigma^+$ Rydberg state. A Pellin-Broca prism separated the fundamental from the frequency-doubled beam. Laser radiation at 226 nm passed through the sampling medium with a beam diameter of 0.5 mm and its intensity was monitored with a photodiode (Pomona Electronics 2390).

LIF emission was collected at right angles to the excitation beam. The optical set-up for LIF collection allowed spatial resolution of the fluorescence, that is, only the emission from a given point source in the flame or flowcell was detected. Figure 16 shows a schematic diagram of the optical set-up necessary to attain spatial resolution. A lens of focal length f_1 is positioned so that the point to be imaged is a distance f_1 away. This allows collimation of the image onto a second lens which focuses the image on an aperture at a distance f_2, the focal length of lens 2. A third lens transfers the LIF image onto the monochromator slit (100μm). Maximum collection efficiency was possible by matching the f numbers (slit aperture/focal length) of lens 3 and monochromator.
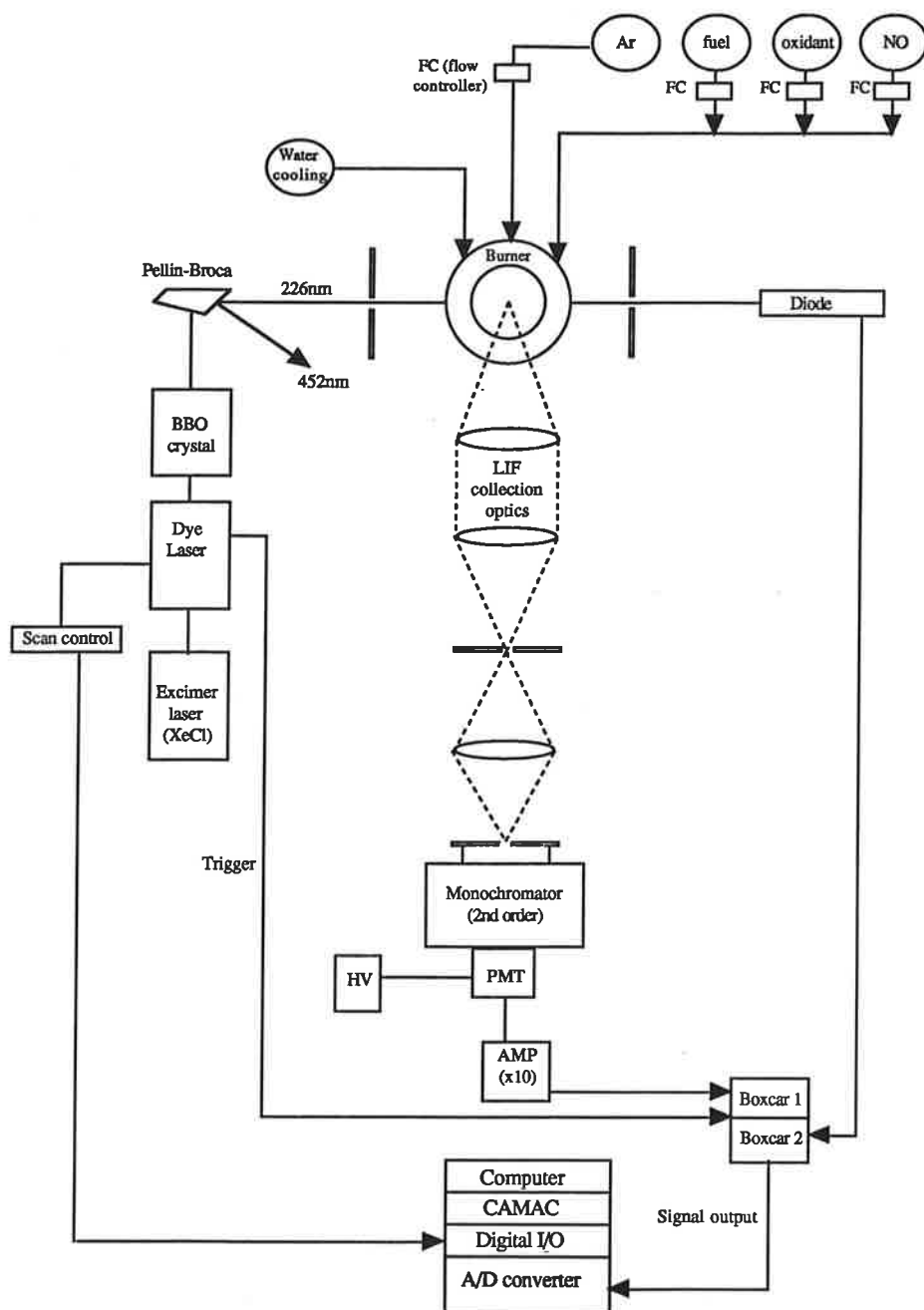
Fig. 15 Experimental set-up used in the rotational energy transfer experiments. The set-up shown above corresponds to that used in the flame experiments. Flow cell experiments used the same laser and detection schemes but replaced the burner system with a flow cell where nitric oxide and the colliders were fed at room temperature.

Light reaching the monochromator (McPherson, 500 nm blaze operated in second order) was then dispersed and collected with a solar-blind (i.e. not sensitive to visible light) photomultiplier tube (Hamamatsu R166) and the signal amplified by a factor of ten prior to collection.
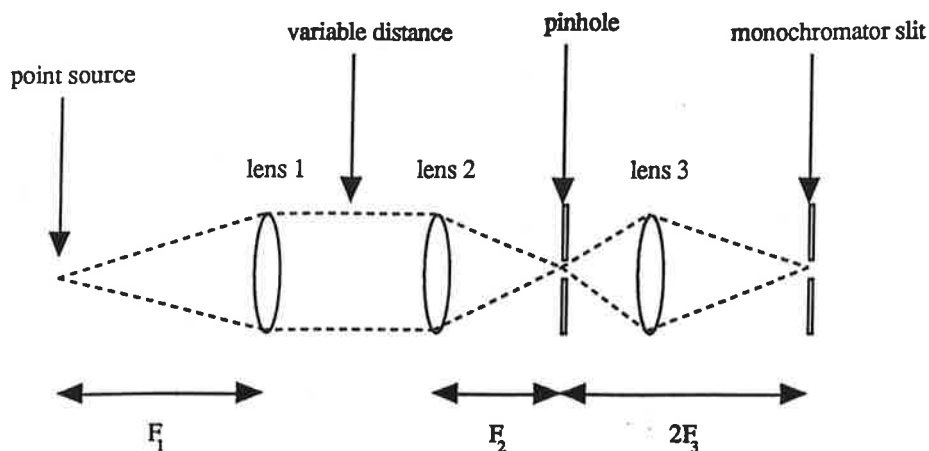
Fig. 16 Optical set-up used to attain spatial resolution of the LIF.

Two boxcar integrators (Stanford Research Instruments) triggered by the dye laser were used for gated detection of the photodiode (laser intensity) and photomultiplier (LIF) signals. In all cases the whole LIF decay signal was collected. This required a gate width of 30 nanoseconds in the flame and up to 200 nanoseconds in the flow cell. Each point was the result of averaging one hundred individual laser shots. Laser intensity data was collected similarly and then used to normalize the LIF signals as will be explained in section 3.1.5.

A CAMAC crate (DSP 6000μP) processed the signals and transferred them to a computer (PC486) for storage. Both laser and monochromator wavelengths were computer-controlled.

Gases were fed into the burner and cell and their flows regulated by flow

controllers (Tylan General FC-280 series). They included the fuel (CH_4 or H_2), oxidant (O_2 or air) and the seeded NO (95%He/5%NO mixture). Argon was used as a protective shroud in the flame experiments.

3.1.2. Flame settings.

Three flames with a fuel/oxidant ratio approximately stoichiometric were studied. Tables I-III display the experimental flows in all three cases. Fuel/oxidant ratios were calculated from the following chemical equations:

$$methane\text{-}oxygen: CH_4 + 2O_2 \rightarrow 2H_2O + CO_2 \qquad (37)$$

$$methane\text{-}air: CH_4 + 2O_2 \rightarrow 2H_2O + CO_2 \\ [O_2 = 0.21\,air] \qquad (36)$$

$$hydrogen\text{-}oxygen: 2H_2 + O_2 \rightarrow 2H_2O \qquad (38)$$

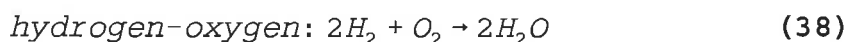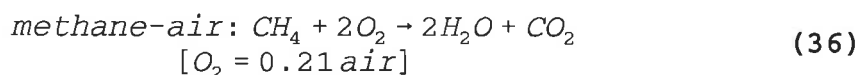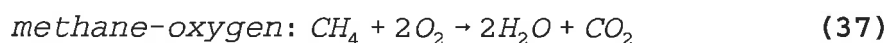Gas flows were chosen so as to provide a stable flame at atmospheric pressure. For example, a much larger flow of air than pure oxygen is necessary to generate a stable CH_4/air flame since O_2, the oxidizer, is only 21% of the total air flow. Both methane flames had a deep blue color and were easily controlled. The H_2/O_2 flame posed additional complications. Since the major combustion product is H_2O, the flame is nearly invisible. It is only possible to see weak red emission in the burnt gases originated from overtone vibrational bands of H_2O. Furthermore, H_2 is a highly explosive gas in the presence of air. These difficulties were overcome by starting with methane fuel and slowly turning the hydrogen flow on. Nitric oxide diluted in He was seeded into the flame at low concentrations, typically 0.04-0.08% of the total flow.

Table I. CH$_4$/O$_2$ flame flows.

Rotational line	CH$_4$ (slpm) (a)	O$_2$ (slpm)	NO (sccm) (b)	Ar (slpm)
P$_{22}$(7.5)	1.7	3.5	4.3	9.2
Q$_{11}$(19.5)	1.7	3.5	4.3	9.2
P$_{22}$(38.5)	1.7	3.5	4.3	9.2

a. slpm=standard liters per minute.
b. sccm=standard cubic centimeters per minute.

Table II. CH$_4$/air flame flows.

Rotational line	CH$_4$ (slpm)	air (slpm)	NO (sccm)	Ar (slpm)
P$_{22}$(7.5)	1.0	9.3	4.4	9.6
Q$_{11}$(19.5)	1.0	9.3	4.4	9.6
P$_{22}$(38.5)	1.1	9.3	4.3	9.9

Table III. H$_2$/O$_2$ flame flows.

Rotational line	CH$_4$ (slpm)	air (slpm)	NO (sccm)	Ar (slpm)
P$_{22}$(7.5)	3.4	1.6	4.3	6.8
Q$_{11}$(19.5)	3.4	1.6	4.3	6.8
P$_{22}$(38.5)	3.4	1.6	4.3	6.8

Three different rotational bands in the (0,0) A-$^2\Sigma^+$–X-$^2\Pi$ system were pumped for each flame: P$_{22}$(7.5), Q$_{11}$(19.5) and P$_{22}$(37.5) at energies 44082.33 cm^{-1}, 44228.00 cm^{-1} and 44216.27 cm^{-1} [56]. Emission spectra were collected by scanning the monochromator (0.2Å stepsize) over the (0,1) band around 2370Å [101]. The monochromator operated in second order thus halving the effective stepsize of the monochromator. Table IV shows a summary of the experimental conditions and lines pumped in the study of all three

flames.

Figures 17-18 show an excitation scan of the (0,0) A-$^2\Sigma^+$←X-$^2\Pi$ band previously taken in a low-pressure propane flame [102]. The three lines used in the atmospheric flame and flow cell study are indicated with arrows. Spectral identification of these individual rotational lines was achieved by scanning the laser wavelength through the NO spectrum using wide bandpass detection (usually 4 nm) and comparing the spectrum to that shown in figures 17-18. The spectrum shown in figures 17-18 was taken using an autotracker system which enables one to scan the laser wavelength and maintain the doubled output intensity by rotating the doubling crystal. Such set-up was not used in the rotational energy transfer experiments; the crystal was rotated manually while varying the laser wavelength thus restricting scans to very small spectral regions at a time (usually 0.1-0.2 nm).
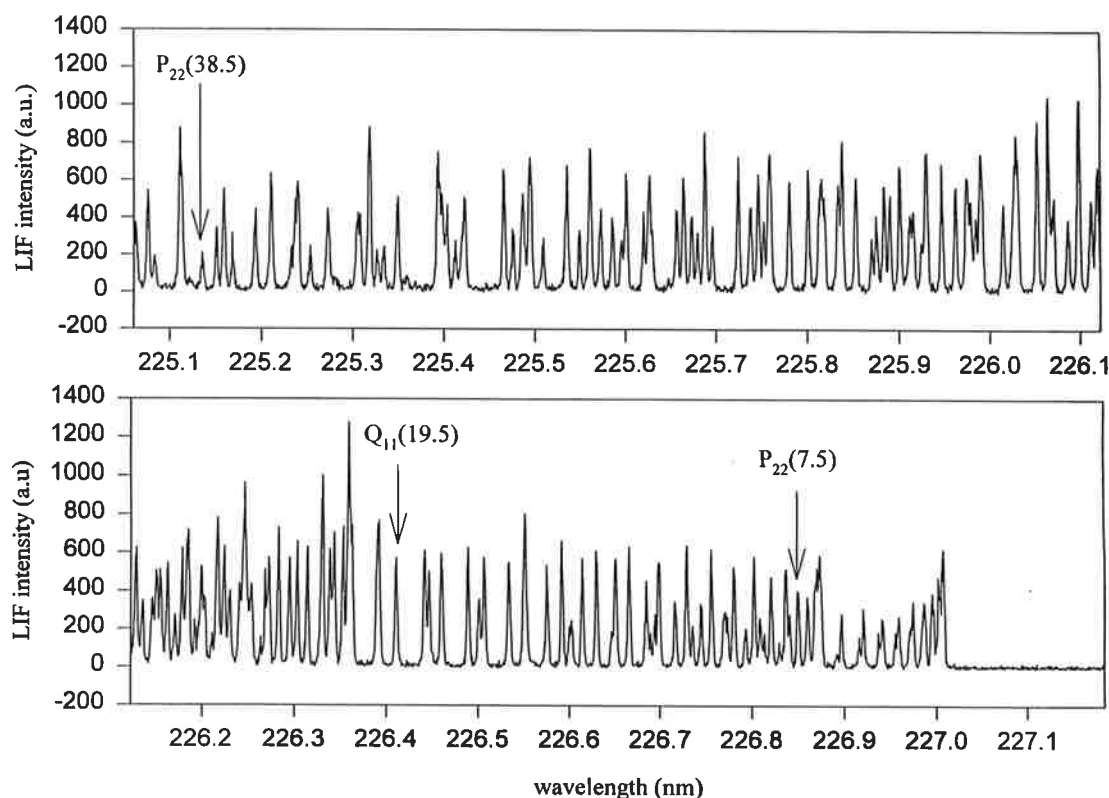
Figs. 17-18 Excitation scan of the (0,0) A-$^2\Sigma^+$ ← X-$^2\Pi$ band of NO. The lines used in the flame and flow cell experiments have been indicated by arrows. They include a low (J"=7.5), medium (J"=19.5) and high (J"=38.5) rotational quantum numbers.

3.1.3 Flow cell settings.

The same set-up as shown in figure 15 was used in the flow-cell experiments. The sintered-brass, water-cooled burner was replaced by a flow cell at room temperature. NO was fed into the flow cell along with different amounts of N_2 and CO_2. Only the $P_{22}(7.5)$ and $Q_{11}(19.5)$ lines were pumped. For a temperature of 298K, levels above $J''=20$ are not sufficiently populated to allow direct pumping.

Emission spectra at different collider pressures were taken as explained before in section 3.2. below. Table V summarizes the experimental conditions. A total pressure measured with a Baratron capacitance manometer is quoted. Due to the small amounts of NO seeded into the flow cell the correction from total pressure to collider pressure is very small.

Table IV. Flame fuel/oxidant ratios and % NO of total flow.

Flame	Fuel/oxidant ratio	Rotational line pumped.	% NO total flow.
CH_4/O_2	0.96	$P_{22}(7.5)$	0.08
CH_4/O_2	0.96	$Q_{11}(19.5)$	0.08
CH_4/O_2	0.96	$P_{22}(38.5)$	0.08
CH_4/air	1.02	$P_{22}(7.5)$	0.04
CH_4/air	1.03	$Q_{11}(19.5)$	0.04
CH_4/air	1.13	$P_{22}(38.5)$	0.04
H_2/O_2	1.04	$P_{22}(7.5)$	0.08
H_2/O_2	1.03	$Q_{11}(19.5)$	0.08
H_2/O_2	1.04	$P_{22}(38.5)$	0.08

Table V. Flow cell settings.

Collider	Rotational line pumped	Pressure range (Torr)
N_2	$P_{22}(7.5)$	0.3-98
N_2	$Q_{11}(19.5)$	1.0-500
CO_2	$P_{22}(7.5)$	1.0-100
CO_2	$Q_{11}(19.5)$	1.0-100

3.1.4. Wavelength calibration with Hg.

Wavelength calibration of all the emission spectra was achieved by looking at the 6^3P_1-6^1S_0 transition in Hg at 2537Å [103]. The experimental emission spectra were corrected by determining the offset between the wavelength measured for Hg and the real wavelength. Figure 19 shows the atomic line corresponding to the Hg transition. From its FWHM it was possible to determine the bandpass of the monochromator: 1.1Å.

3.1.5. Saturation tests.

LIF intensities normalized for laser power fluctuations, are an indirect measure of the relative population of the initial level. Then one only needs the line strength of the transition to make the conversion from intensity to relative population.

However, for this to hold true one must work below saturation levels, that is, the LIF signal has to be linear with respect to both laser power and electronic gain. In an experiment like the one described here there are various sources of saturation. The most common ones are intensity and detector saturation.

For example, if the laser intensity is very large then one can saturate the transition; the LIF intensity corresponding to such transition shows sub-linear behavior with respect to laser power, thus yielding an underestimate of the population in this level. Figure 20 shows a typical saturation test performed in the CH_4/O_2 flame. The monochromator was

positioned at the emission maximum around 2370Å while pumping the $P_{22}(7.5)$ transition. Each point in the graph is the statistical average of about three hundred individual measurements under the same conditions. The error bars are quite small, less than two percent of the total LIF signal. The LIF trend with laser power is linear, allowing us to use the spectra to obtain excited state rotational populations.
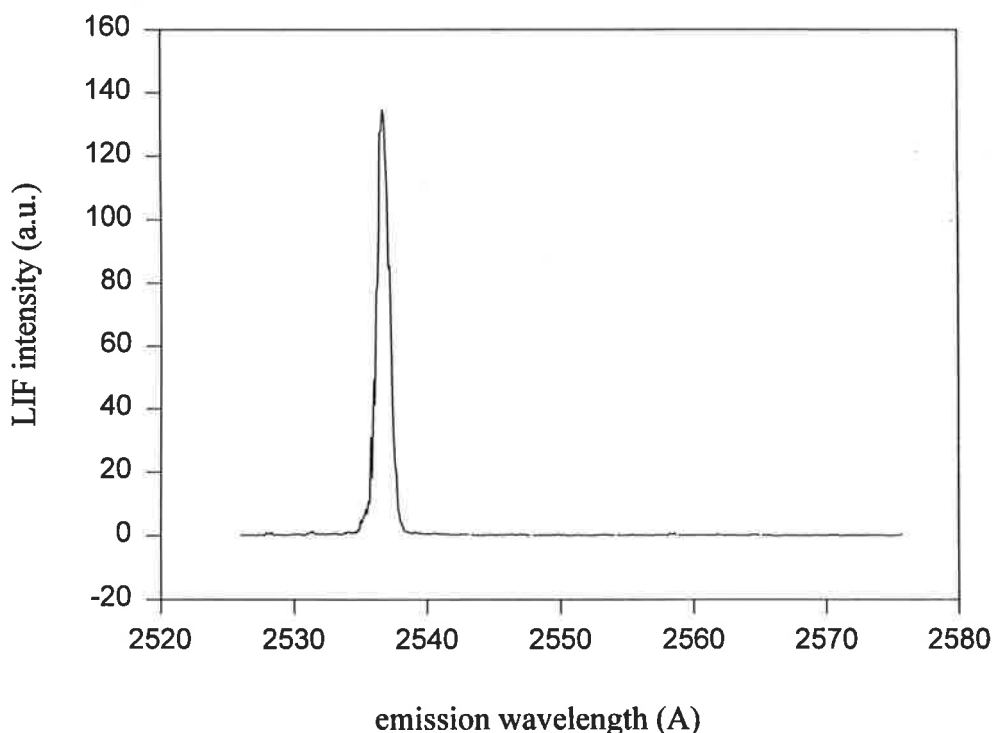
Fig. 19 LIF emission spectra of the $6^3P_1 \leftarrow 6^1S_o$ transition of Hg at 2537Å
used for wavelength calibration of the flame and flow cell spectra.

Similarly, saturation of the detection set-up is also possible if the collected signal is large enough to induce a non-linear photomultiplier response. Then the signal generally appears flat or nearly flat regardless of which rotational line one is detecting and the temporal evolution of the LIF signal with time cannot be represented by a single exponential decay. Figure 21 shows an emission spectra suspect of suffering from saturation. The most intense peaks appear clipped and flat at the top suggesting a non-linear response of the detection system. In general, this type of saturation was avoided by looking at the photomultiplier current to ensure that it stayed within the maximum ratings

-55-

specified by the manufacturer, usually 0.1mA, and also by checking linear behaviour of the PMT in an analogous manner to that expalined above and shown in figure 20.
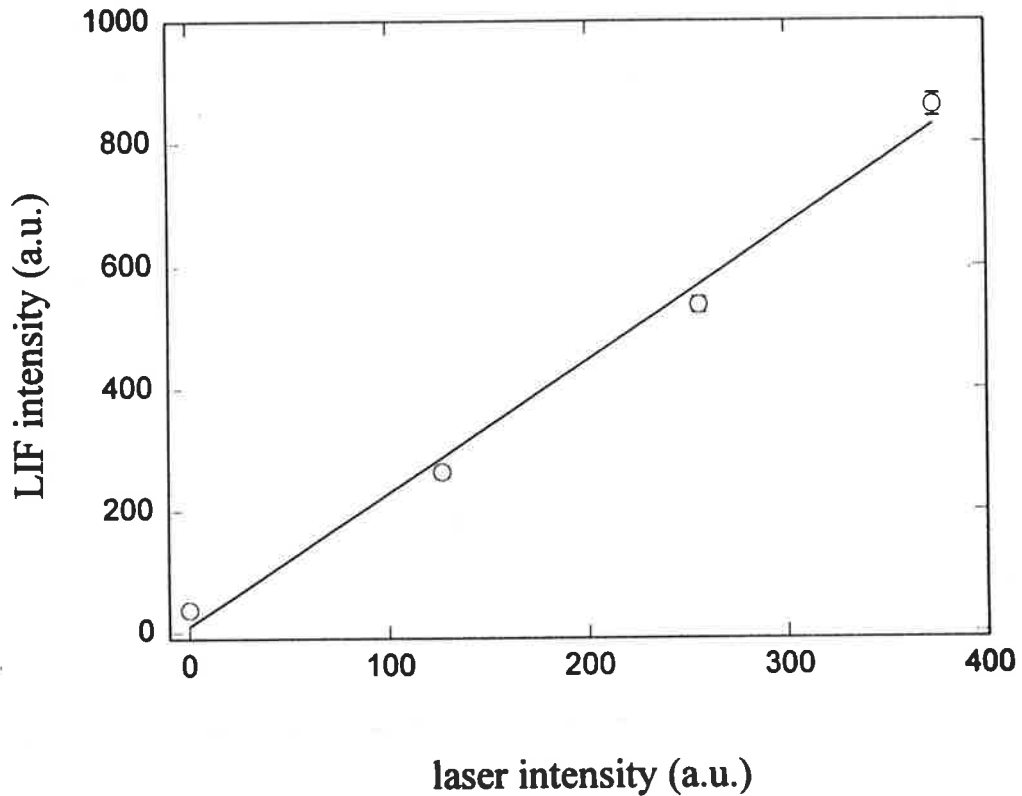
Fig. 20 Laser saturation test performed in a CH_4/O_2 flame. Each point corresponds to the average of about three hundred points taken under identical experimental conditions. The plot shows a linear behavior of the LIF signal with laser power.

3.2. Experimental results.

3.2.1. Flame emission spectra.

Figure 22 shows one of the flame spectra with the bandhead positions of the all rotational transitions emitting from the excited state. The notation is the same as explained in section 1.2.5. Analogous to absorption, there are a total of twelve rotational branches originating from the emission of the excited state.

Figures 23-31 show the emission spectra for the three different pump lines and

flame environments. Wavelengths have been normalized using the mercury standard described in section 3.1.4. All spectra have been corrected for laser power fluctuations and scaled to the same total integrated signal to allow their comparison.

Spectra corresponding to the same rotational level look very much alike. In all cases they appear peaked at the initially-pumped level with little intensity arising from additional rotational transitions.
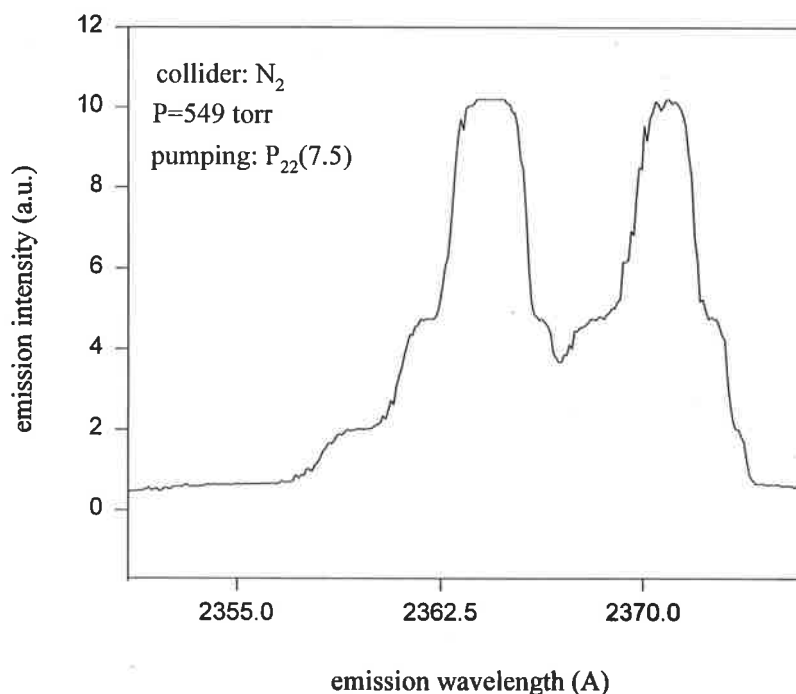
Fig. 21 Emission spectra of the (0,1) X-$^2\Pi$←A-$^2\Sigma^+$ band of NO in the presence of N_2 at a total pressure of 549 torr in a room temperature flow cell. The spectra shows the typical features of a saturated sample, i.e. flat intensity maxima and broad and structureless features.

3.2.2. Flow cell emission spectra.

Emission spectra for N_2 are shown in figures 32-41 for $P_{22}(7.5)$ and 42-50 for $Q_{11}(19.5)$. CO_2 data is shown in figures 51-57 and 58-66. They have all been normalized to laser power fluctuations and scaled to the same total integrated signal as explained for

the flame spectra in section 3.2.1.

Even to the naked eye, N_2 and CO_2 show markedly different behavior with increasing pressure. N_2 spectra change drastically up to a total pressure of 10 torr. After 10 torr, the emission spectra do not seem to change any further. CO_2, on the contrary, shows little change with pressure. Spectra at 10 torr and 100 torr look essentially the same. This behavior is specially apparent for the $Q_{11}(19.5)$ line. High-pressure CO_2 spectra are noisier due to the small fluorescence quantum yield and consequently a lesser number of photons being detected.
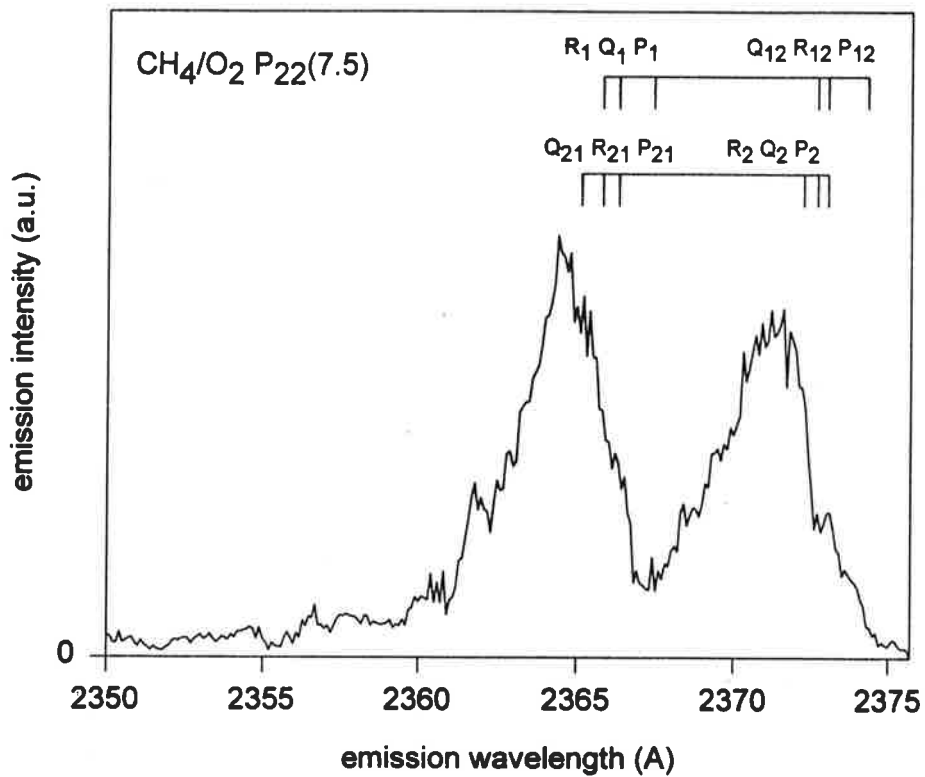
Fig. 22 Emission spectrum of the $(0,1)$ A-$^2\Sigma^+$ ← X-$^2\Pi$ NO band pumping $P_{22}(7.5)$ in a CH_4/O_2 flame showing the bandhead positions of all twelve possible rotational branches.
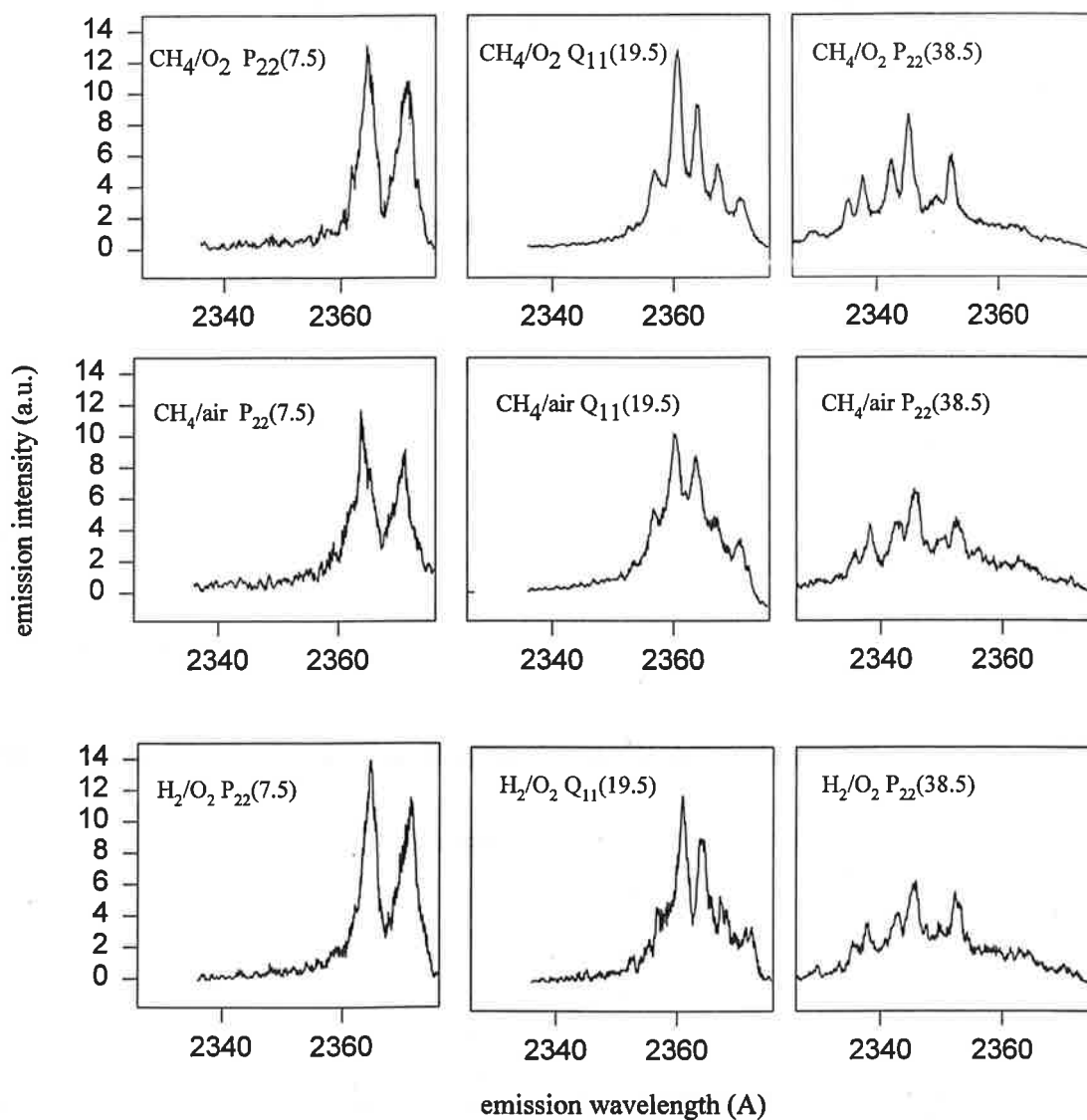
Figs. 23-31 Flame emission spectra of the (0,1) $A\text{-}^2\Sigma^+\text{-}X\text{-}^2\Pi$ NO system. Rows correspond to a given flame while each column represents a different rotational transition.
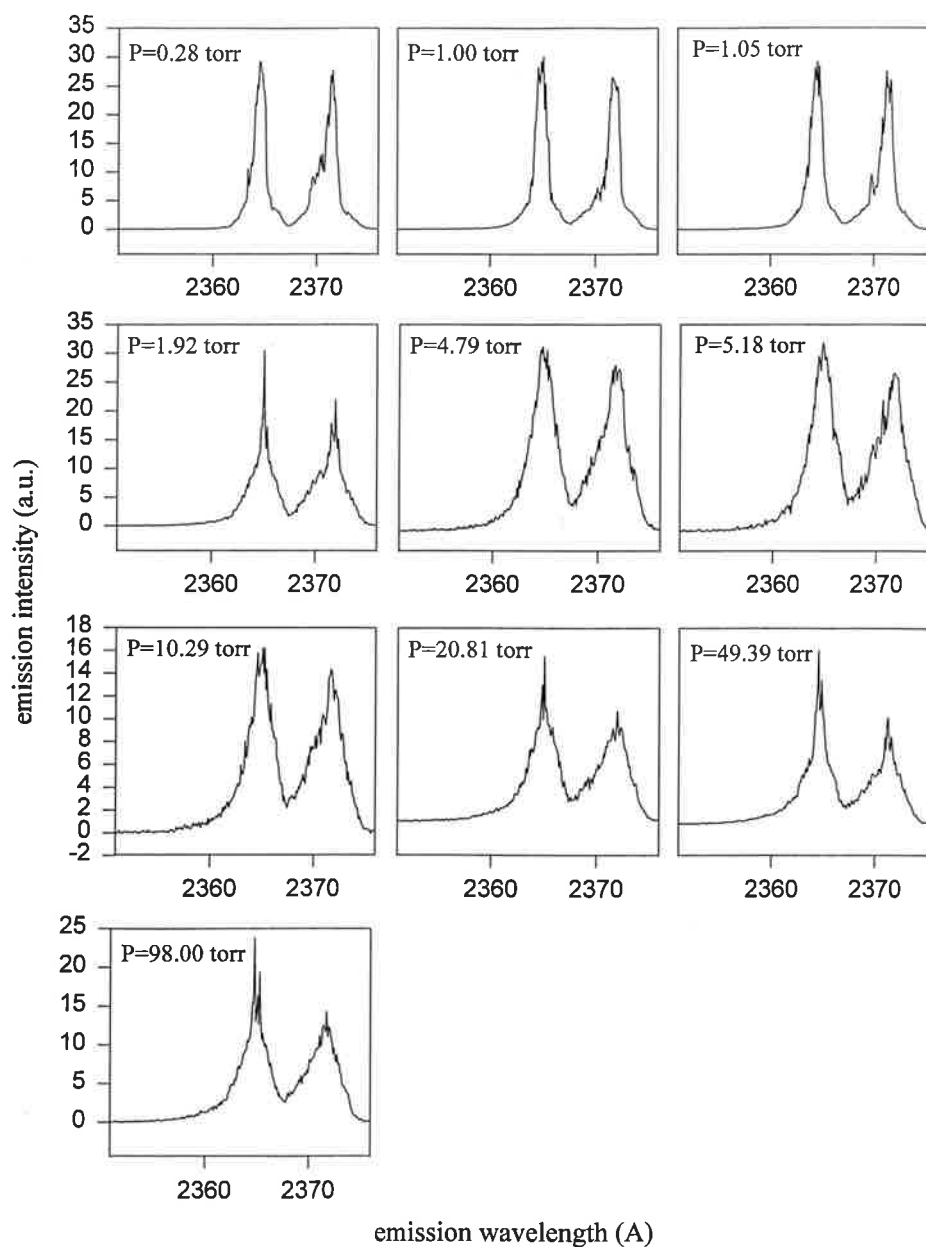
Figs. 32-41 Room temperature emission spectra of the (0,1) A-$^2\Sigma^+$-X-$^2\Pi$ NO system pumping the $P_{22}(7.5)$ rotational transition at different N_2 pressures.
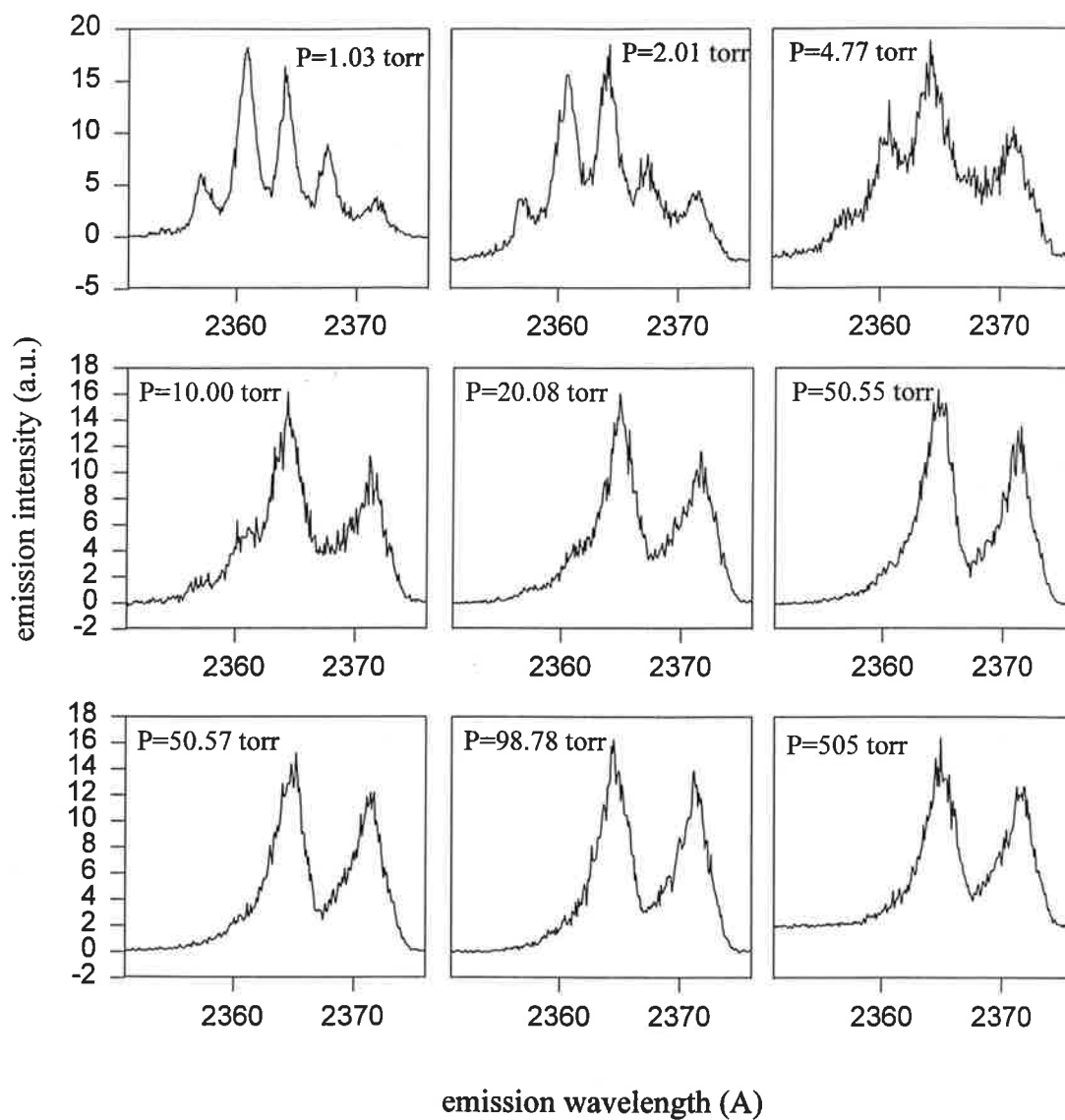
Figs. 42-50 Room temperature emission spectra of the (0,1) $A\text{-}^2\Sigma^+\leftarrow X\text{-}^2\Pi$ NO system pumping the $Q_{11}(19.5)$ rotational transition at different N_2 pressures.
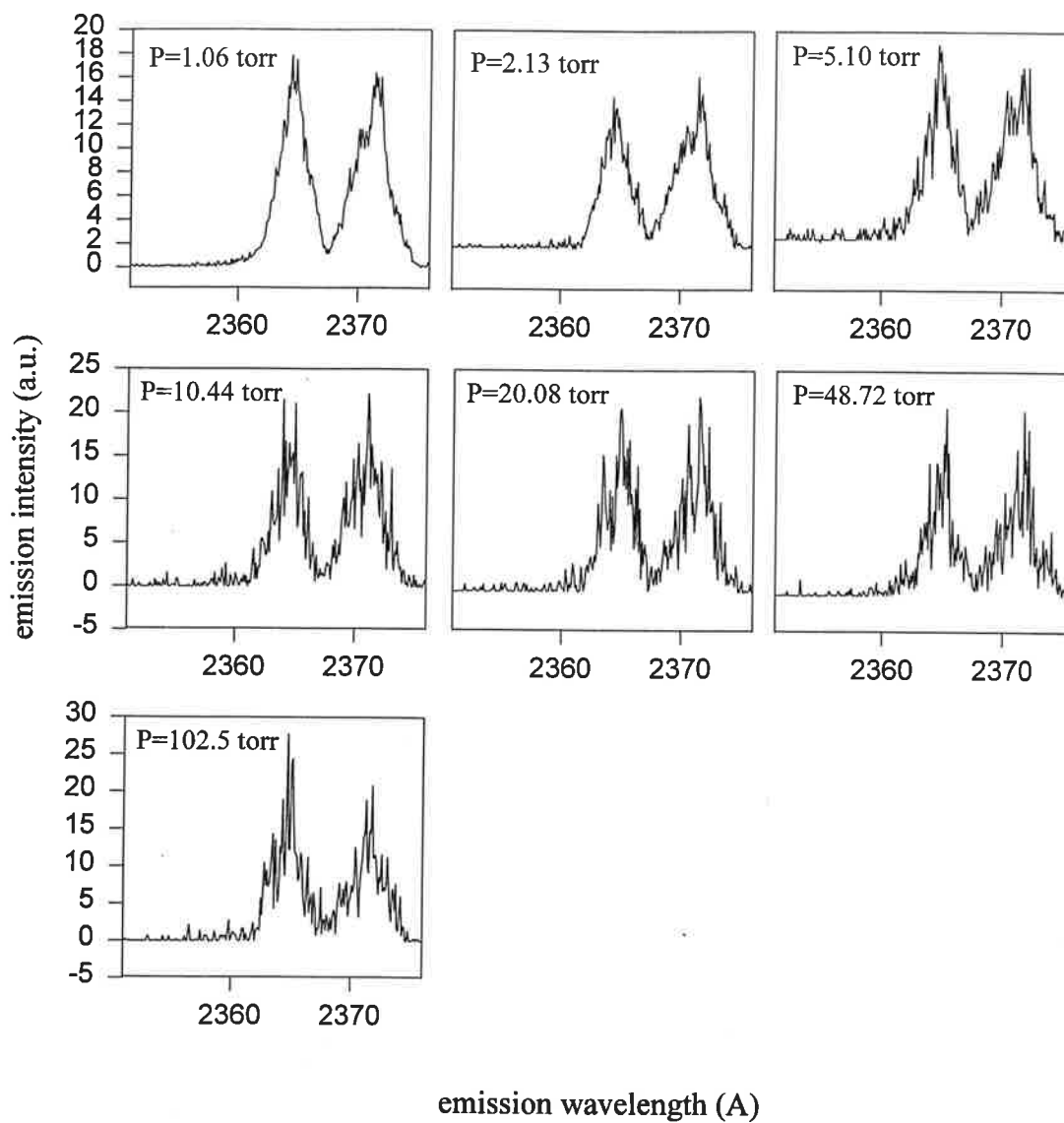
Figs. 51-57 Room temperature emission spectra of the (0,1) $A\text{-}^2\Sigma^+\leftarrow X\text{-}^2\Pi$ NO system pumping the $P_{22}(7.5)$ rotational transition at different CO_2 pressures.
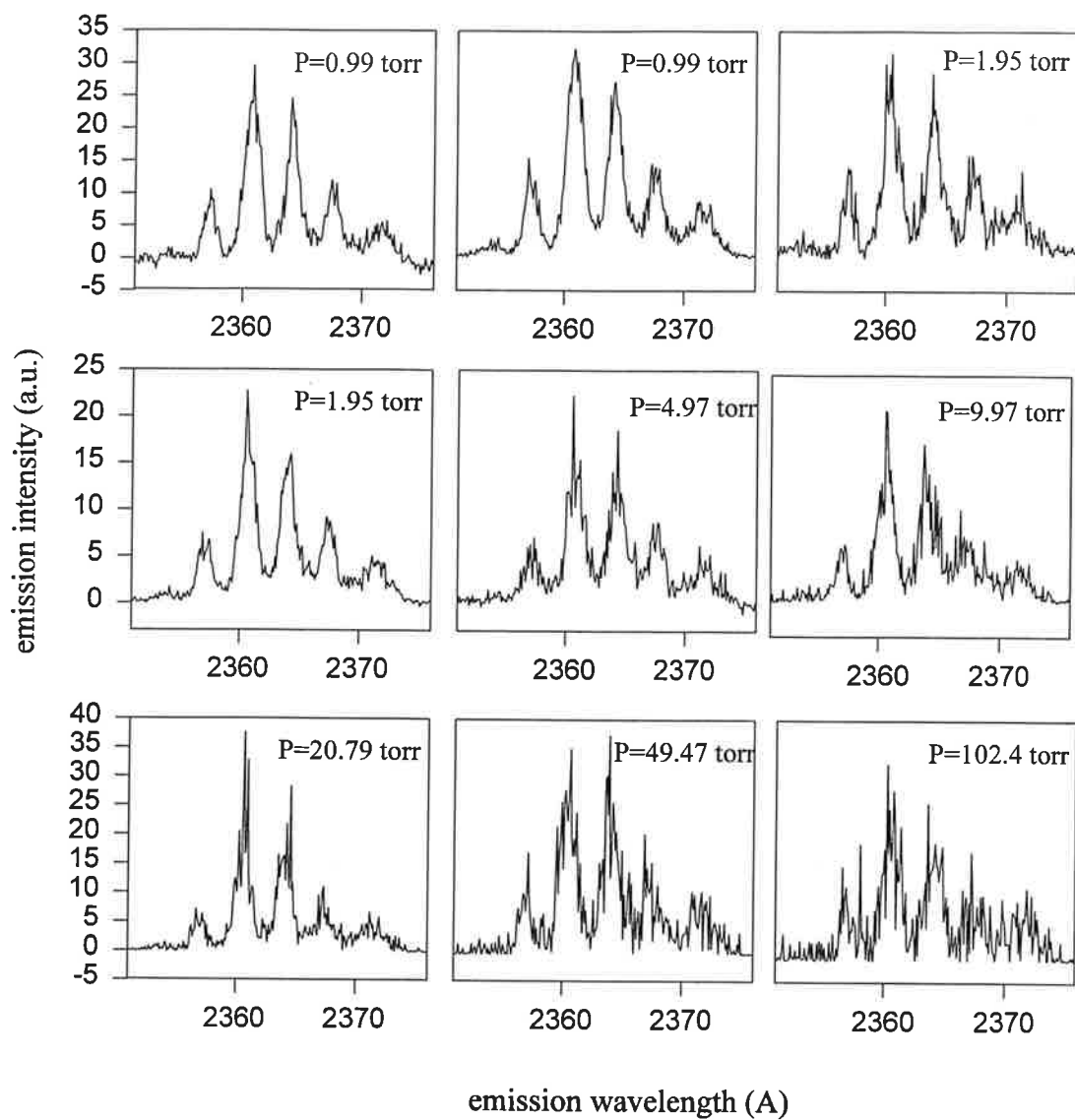
Figs. 58-66 Room temperature emission spectra of the (0,1) A-$^2\Sigma^+$-X-$^2\Pi$
NO system pumping the $Q_{11}(19.5)$ rotational transition at different CO_2
pressures.

3.3. Analysis of experimental results.

3.3.1. Spectral simulation.

The emission spectra shown in section 3.2 provide an indirect way of looking at the rotational population in the excited state. If the rotational line strengths, or transition probabilities, are known then it becomes straightforward to relate LIF intensities to rotational populations. As simple as this task might seem, the closeness of rotational transitions for a molecule like NO complicates matters. With our experimental resolution it was not possible to discriminate individual rotational transitions in emission. Full rotational resolution is generally possible for diatomic anhydrides such as OH or CH with large rotational constants, i.e. the rotational constant provides a rough measure of the distance between rotational lines in the spectrum. NO has a rotational constant in the A-$^2\Sigma^+$ state roughly ten times smaller than OH resulting in an inevitable clumping of rotational spectral lines. This problem can be partially circumvented by the use of spectral simulation programs. A number of them are available for absorption [104,105] and emission spectra [106]. The inputs to the programs are an *a priori* rotational distribution and the experimental spectral resolution. The program output is the spectrum calculated from a knowledge of line positions, Hönl-London factors, and line broadening parameters.

3.3.1.1. Flame spectra.

A preliminary analysis of the flame data using the simulation program LIFBASE [106] showed that the low-J spectra could be satisfactorily fit to a thermal distribution at 280K, corresponding to a J'_{max}=6.5. For J'=19.5 and 37.5 the emission remains peaked at the initial level with the populations necessary to fit the experimental spectra highly non-Boltzmann. For J'=19.5 the distributions were approximately symmetrical with respect to the initially pumped level while for J'=37.5 leakage into J<37.5 predominated. At this point, these results are only qualitative. More conclusive results about the shape of the rotational populations rising from the medium and high-J pumped levels are currently

underway along with an analysis of the performance of different mechanisms in reproducing the experimental emission spectra
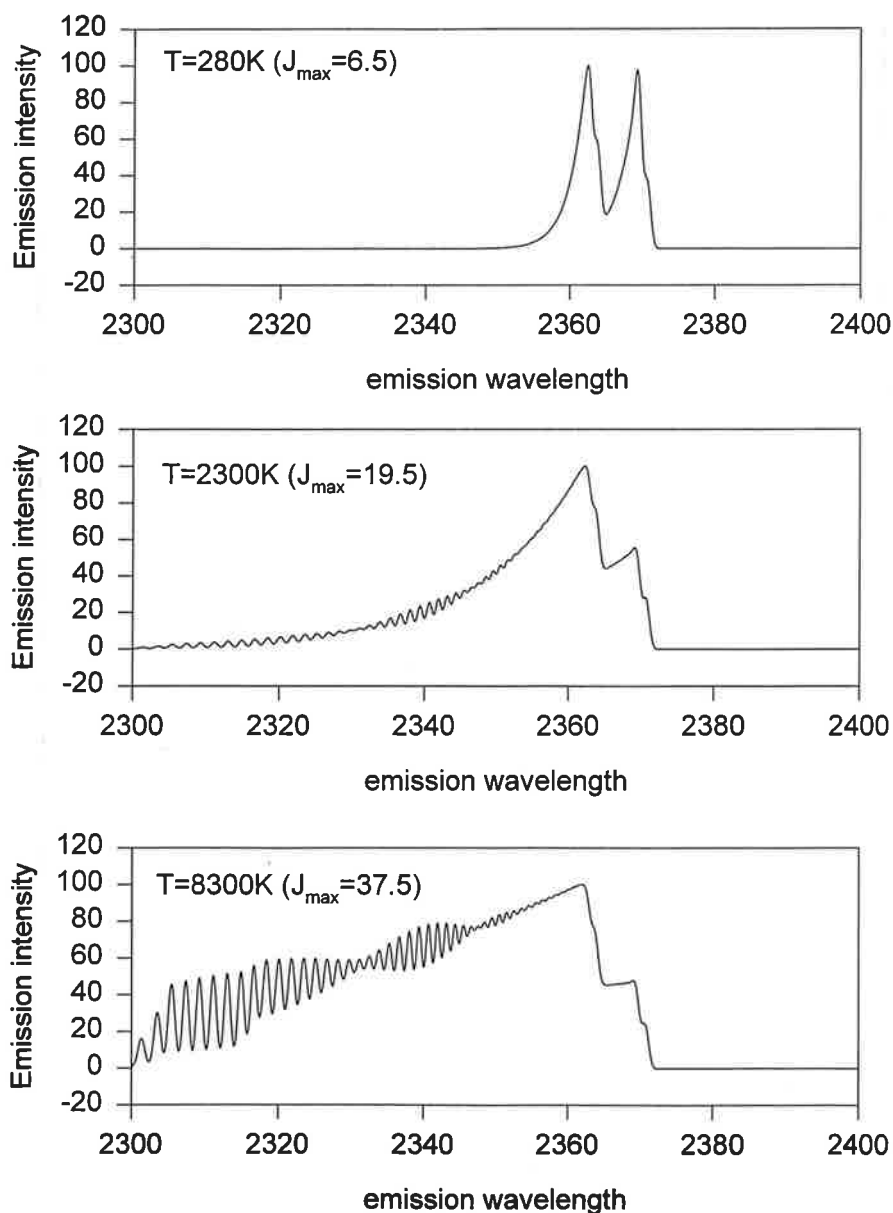
Figs. 67-69 Simulated spectra of the (0,1) $A-^2\Sigma^+ \leftarrow X-^2\Pi$ NO band at different temperatures with J_{max} corresponding to the rotational levels pumped in the flame experiments. Compare these spectra with figures 22-30; only the low-J spectra appear to be very similar in both cases.

Figures 67-69 show a set of three simulated thermal spectra with J_{max} equal to 6.5, 19.5 and 37.5 respectively. Only in the case of J'=6.5 there is any similarity between simulation and experiment.

3.3.1.2. Flow cell spectra.

N_2 spectra at pressures higher than 10 torr satisfactorily fit a thermal distribution circa 300K, corroborating our previous qualitative observation that spectra did not change above 10 torr. This finding suggests that thermalization has been attained, that is, at pressures above 10 torr there is a sufficient number of collisions to reach thermalization of the excited state rotational population.

Use of the simulation program has, however, severe limitations if we are to look for quantitative differences in the non-Boltzmann experimental data. The primary input to the simulation is the rotational distribution of the excited state, precisely one of the pieces of information unknown to us. If, as in our case, there is not enough *a priori* knowledge of the population distribution, except maybe for those spectra that look strikingly thermal, then the procedure becomes more a matter of guesswork.

Furthermore, matters are complicated by something we have disregarded so far: line overlap in the excitation spectrum. The spin orbit coupling in the A-$^2\Sigma^+$ state is so small that the laser bandwidth, approximately 0.25 cm^{-1}, is not able to discriminate between the pumping of either spin-orbit state in the A state. For example, pumping $P_{22}(7.5)$ which goes into J'=6.5 in the F_2 spin orbit state will also excite $Q_{12}(7.5)$ populating J'=7.5 in F_1. How much each excited state level is populated is given by the relative ratio of line strengths for these two transitions. In this particular case both transitions have similar strengths and thus both J'=6.5 in F_2 and J'=7.5 in F_1 will be equally populated. Similarly, $Q_{11}(19.5)$ overlaps with $P_{21}(19.5)$ with a population ratio of 86% versus 14% respectively and $P_{22}(38.5)$ with $Q_{12}(38.5)$ in a ratio of 87% to 13%.

Simultaneous simulation of rotational relaxation with two initial rotational levels pumped makes the problem intractable. Moreover, there is no data available on the probability of population leaking from one spin orbit state to another, adding an extra

unknown to the overall problem.

Simulation proved to be useful in two respects. First it corroborated that the flow cell data at high pressures is actually thermalized, i.e. rotational energy transfer is complete. Second, it enabled us to make an important empirical finding, namely, that in the flame environments it may be possible to obtain thermal emission spectra for 'temperatures' that cannot correspond to true flame temperatures.

3.3.2. Analysis of spectra by the method of residuals.

From the simulations it was possible to obtain vital information for carrying a more quantitative analysis of the emission spectra. Of particular importance was the capabilitiy of N_2 to thermalize the excited state rotational population at room temperature.

A standard procedure to check how different two spectra are from each other involves calculating the square of the sum of the residuals [107]. By residuals is meant the difference in fluorescence signals at a given point for two spectra that have been power-corrected, normalized to the same total integrated signal and cover the same spectral range. If $S_\lambda{}^1$ is the LIF normalized signal at wavelength λ from spectrum 1 and $S_\lambda{}^2$ is the signal from spectrum 2 at that same wavelength then R^2 is given by:

$$R^2 = \Sigma_{i=\lambda_0,\lambda_f} (S_i^1 - S_i^2)^2 \qquad (39)$$

Where λ_0 and λ_f denote the initial and final wavelengths over the spectral range considered. Squaring the difference in signals ensures that no fortuitous cancellations occur: differences between spectra are accounted for regardless of whether these are positive or negative.
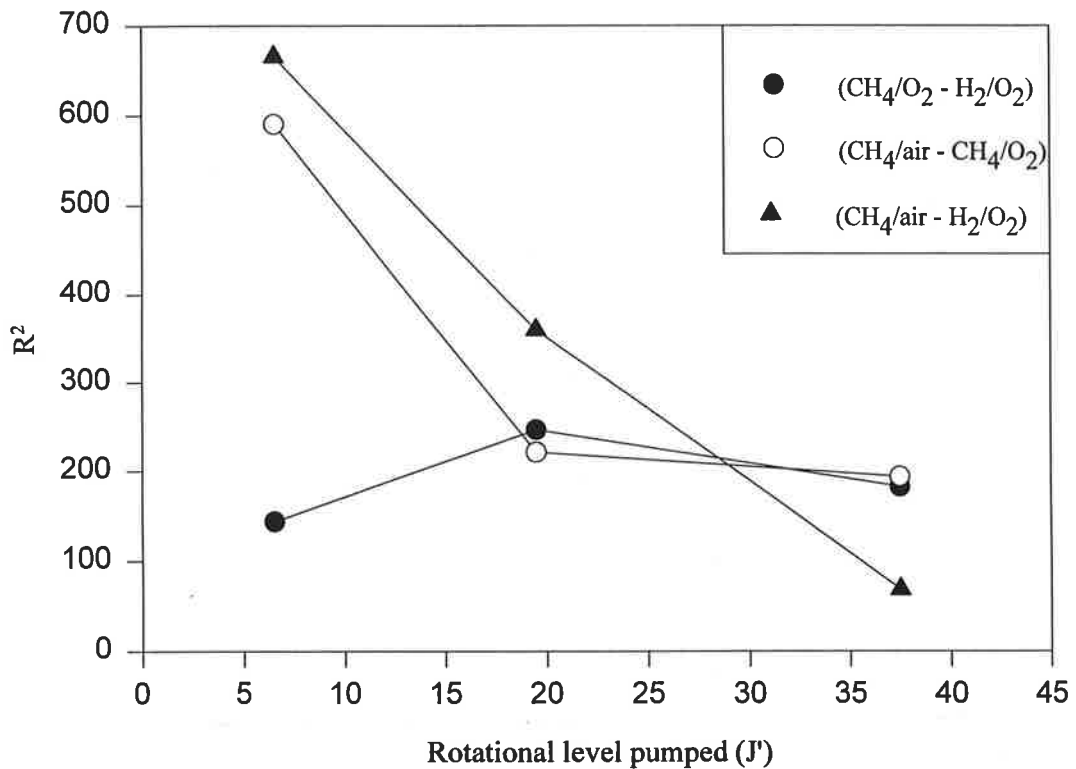
Fig. 70 Residual analysis of the flame emission spectra. The legend indicates what sets of flame data have been compared in each case. Note that only appreciable differences are clear when comparing the CH4/air flame with either of the two oxygen flames.

3.3.2.1 Flame spectra.

Figure 70 shows the results of applying the residual analysis to the flame spectra. All three possible comparisons have been made. As indicated in the legend of figure 70, spectra for a given pump line have been subtracted from those of that same pump line but in a different flame.

Two important trends are discernible from this plot. First, there is a constant

behavior of the residuals obtained from comparing the two oxygen flames over the whole range of rotational numbers studied. This suggests that the collissional environments in the burnt gases of the two oxygen flames are very similar. Second, there is a decrease in residual with rotational number pumped when comparing the CH_4/air with either of the two oxygen flames. Residuals are largest for the low-J runs and decrease with rotational number up to the point, at J'=37.5, where they become indistinguishable from those residuals originating from the comparison of the oxygen flames. This implies that the CH_4/air flame has a collisional environment different from the oxygen flames as well as a change in the extent of thermalization with rotational number since residuals show a consistent decrease with rotational level pumped. A more detailed explanation and rationalization of these two tends will be postponed to section 4.

3.3.2.2. Flow cell spectra.

Figures 71 and 72 show the square of the residuals for N_2 and CO_2 for the two pump lines respectively. This time the plots are of R^2 as a function of total pressure. The reference spectrum, indicated by an arrow in the figures, has been chosen to be common to all calculated residuals. It corresponds to an N_2 emission spectrum at 98 torr which is described by a thermal rotational population at 298K. Deviations from this reference will be indicative of how far a given spectrum is from thermalized.

The N_2 residuals show a clear trend towards thermalisation as the pressure increases. R^2 is large at low pressures but it quickly decreases in an exponential-like fashion. From figures 71 and 72 it is apparent that for $Q_{11}(19.5)$ it takes a higher pressure to reach thermalisation. From these considerations it is possible to furnish an overall rotational relaxation cross section by taking the pressure at which thermalisation is achieved, i.e R^2 converges to a constant value. Such a cross section, σ_R, is given by the following equality:

$$\frac{1}{\tau_{rad}} + k_Q[Q] = k_R[Q] = \sigma_R v_{NO,Q}[Q] \qquad \qquad (40)$$

where τ_{rad} is 217 nanoseconds [67], the radiative lifetime of the zeroth vibrational level of the $A\text{-}^2\Sigma^+$ state and k_Q is the quenching cross section for N_2 at 298K [73]. [Q] is the concentration of N_2 at the pressure where the levelling-off in the residual occurs and $v_{NO\text{-}Q}$ is the relative velocity of the NO-Q pair.

Fig. 71 Residual analysis of the room temperature data for N_2 and CO_2 pumping $P_{22}(7.5)$. The arrow indicates which point was used as a common reference for the determination of the residuals.

The lefthand side of equation 40 corresponds to the total electronic deactivation rate of the excited excite at the collider concentration where convergence to the thermal population is reached. This can be equated to a pseudo rate constant, or cross section, for rotational relaxation. This cross section does not describe a single-collision process as a typical state-to-state cross section would. It can be interpreted, however, as the sum of all those state-to-state cross sections that connect all rotational levels participating in the process of rotational relaxation.
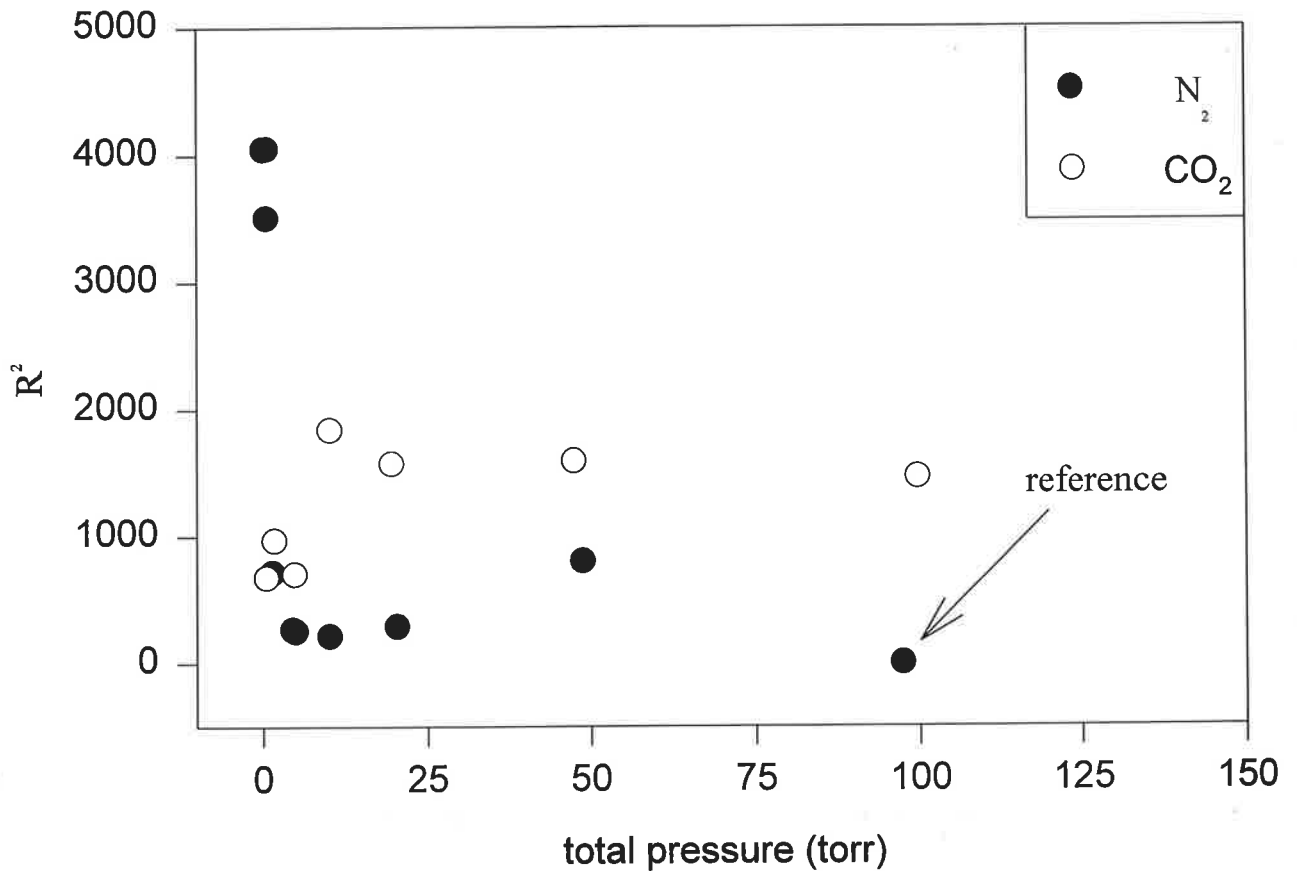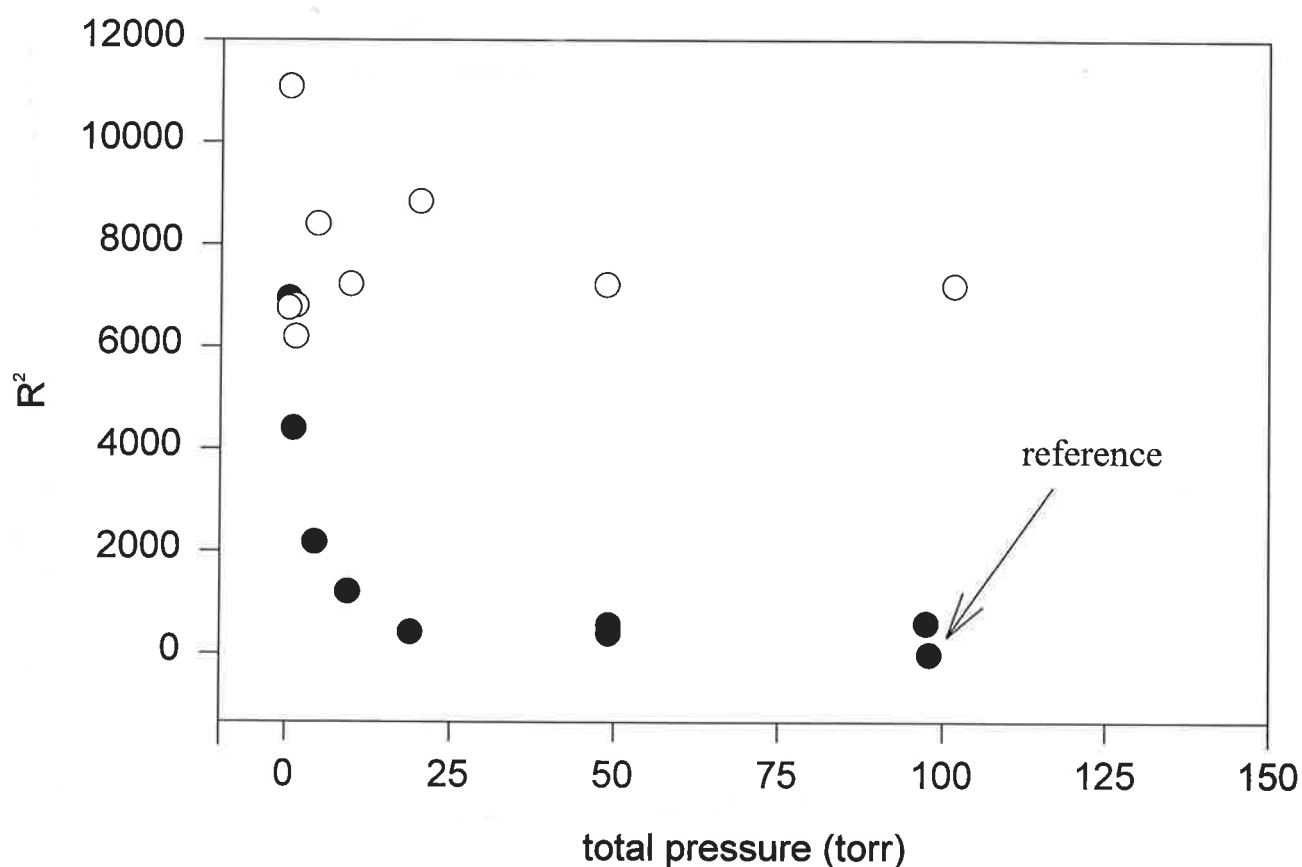

Fig. 72 Residual analysis of the room temperature data for N_2 and CO_2 pumping $Q_{11}(19.5)$. The arrow indicates which point was used as a common reference for the determination of the residuals.

Choosing the pressure at which thermalisation is achieved is not trivial. One could feel tempted to fit a mathematical function, i.e. an exponential, through the experimental points and find the turning point by evaluating where the slope or derivative levels off and from there find the pressure 'turning point'. However, there is no physical model available that can provide us with a functional form to fit the data. Instead, cross sections were estimated for two different experimental points close to the turning point and then averaged to furnish a total rotational relaxation cross section. For $J'=6.5$ it is approximately 10Å^2 while for $J'=19.5$ it is 2Å^2.

The CO_2 data shows a markedly different behavior. For $P_{22}(7.5)$ the low pressure residuals are closer to the thermal spectrum but they quickly converge to a constant value at higher pressures (fig. 71). In the case of $Q_{11}(19.5)$, the low pressure points have very large residuals, larger than those for $P_{22}(7.5)$ at the same pressure and show some degree of scatter (fig. 72). As the pressure increases such uncertainty decreases and the residuals are consistently higher than those for $P_{22}(7.5)$ throughout the pressure range, i.e. there is less progress towards thermalization. A convenient way of expressing this trend would be to say that all spectra, and therefore rotational distributions, for a given pump line remain 'locked' irrespective of collider concentration.

4. Discussion and conclusions.

When NO is promoted to the zeroth vibrational level of the $A\text{-}^2\Sigma^+$ Rydberg state the competition between radiative emission, quenching and rotational energy transfer determines the appearance of the emission spectra. Both the radiative lifetime and quenching determine the overall lifetime of NO in the excited state. The molecular 'clock' is set at zero when the laser promotes NO to the excited state; the radiative lifetime, τ_{rad}, and $k_Q[Q]$ are responsible for bringing it to a stop. $k_Q[Q]$, or more accurately $\Sigma_i k_{Qi}[Q_i]$, the sum of all quenching processes, is the only parameter one can control by choosing the appropriate collider and temperature. The radiative lifetime, on the contrary, is an upper limit to the lifetime of the excited state impossible to exceed since it is determined by the quantum mechanical characteristics of the particular molecular state.

From these considerations it follows that if one knew the radiative emission lifetime and all rate constants describing the collisional processes deactivating and modifying the excited state then it would be straigthforward to account for the appearance of the emission spectra. Conversely, one can learn about inelastic collisional processes by looking at the emission spectra and their behavior as a function of variables such as collider type, concentration, temperature, and from this hope to develop a picture of the collisional process under study.

The room temperature results for N_2 and CO_2 offer an appropriate starting point to discuss the relative importance of quenching and rotational relaxation in all the systems covered by this study.

4.1 The competition between rotational relaxation and quenching for N_2 and CO_2 at room temperature.

As pointed out in section 3.3.2.2, N_2 appears to be quite efficient at thermalizing the excited state population. This behavior is expected in view of the fact that N_2 is a very poor quencher at room temperature ($\sigma_Q \leq 0.049\pm0.072\text{Å}^2$) [73]. Emission from the

excited state is dominated by a radiative lifetime of 217 nanoseconds [67]. A higher N_2 density will not decrease the lifetime through quenching but will induce more collisions with $NO-A-^2\Sigma^+$ and thus further thermalisation of the excited state rotational population. Figure 73 shows how the effective lifetime of nitric oxide is barely altered by N_2 quenching.
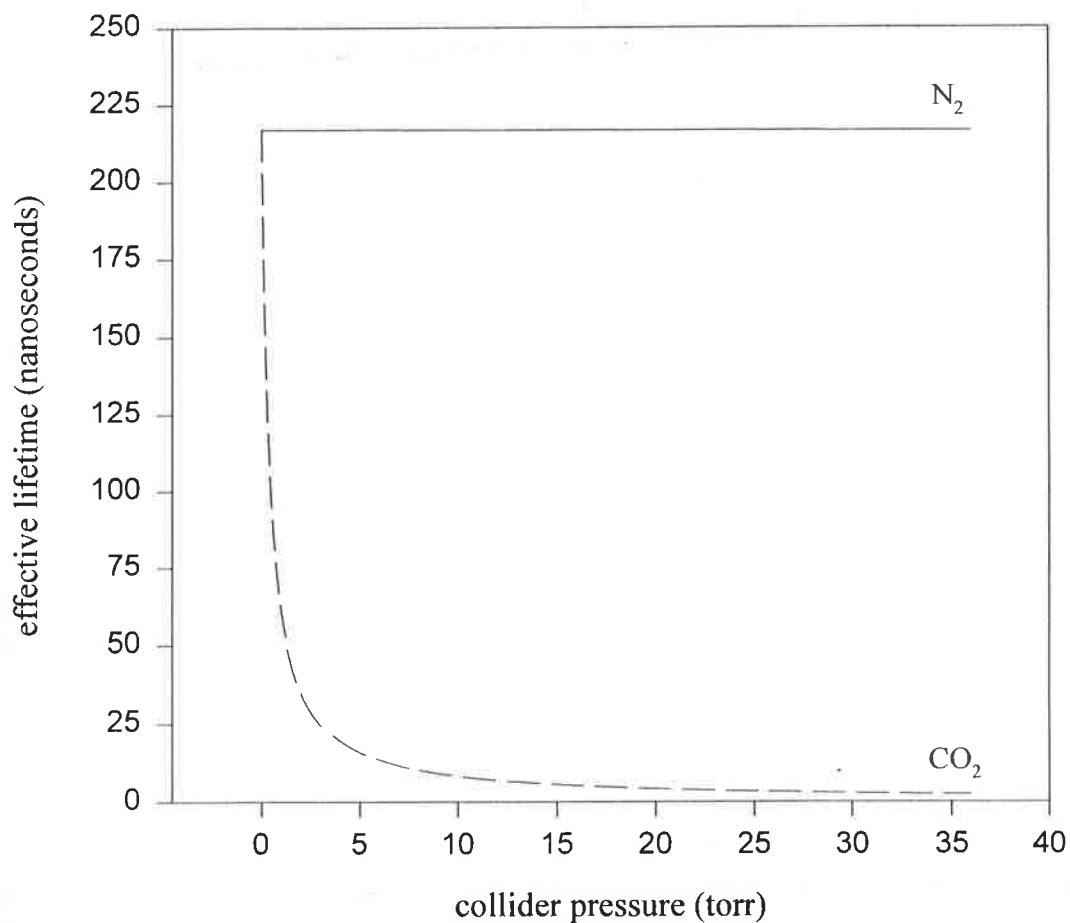

Fig. 73 Effective lifetime of $A-^2\Sigma^+$ NO as a function of collider pressure for N_2 and CO_2 at 298K. Note that only in the CO_2 case the effective lifetime shows a strong dependence on collider pressure.

CO_2, on the contrary, is a very efficient quencher at room temperature (σ_Q = 61.2Å^2) [74] and the excited state lifetime is dominated by this process even at very low collider pressures. In figure 73 the effective lifetime as a function of collider pressure has also been plotted for CO_2. The behavior this time is strikingly different with lifetime, decreasing dramatically as soon as the CO_2 density is increased. Quenching becomes predominant at only 0.3 torr, the pressure at which $k_Q[Q]$ becomes equal to $1/\tau_{rad}$. The lowest experimental pressure is 1.0 torr, sufficient to make the overall quenching rate three times bigger than the radiative rate. A closer look at the CO_2 residuals (figs. 71 and 72) shows a consistent increasing trend of R^2 with pressure below 10 torr. This behavior is difficult to explain in terms of a rotational transfer mechanism since a lower CO_2 pressure would imply, if anything, a lesser extent of thermalisation and therefore a larger R^2!

The solution to this puzzle lies in first considering the meaning of the overall RET cross sections measured in these experiments and second in looking at the effective lifetime of NO A-$^2\Sigma^+$ as a function of CO_2 pressure. The cross sections reported in this work are a measure of the speed of overall rotational relaxation, not individual state-to-state cross sections. Thus, these bulk cross sections do not have to follow a linear behavior with pressure since they are not describing a single collision process. This trend can is also discernable from the N_2 data. Second, as figure 73 shows, around 10 torr the effective lifetime is still significant, i.e. tens of nanoseconds, but it decreases dramatically as the pressure is increased. The constant behavior of R^2 above 10 torr can thus be attributed to the levelling off of the effective lifetime with pressure. Below that pressure, there is still sufficient time for extra thermalization to occur with increasing pressure, so the observed increase in the residuals is plausible.

In the CO_2 quenching-dominated environment NO A-$^2\Sigma^+$ has practically no time to thermalize before it is deactivated by quenching; thus 'locked' emission spectra are observed irrespective of collider pressure. One can then ascribe an upper bound of 61Å^2 to the CO_2 overall thermalisation cross section. If the cross section were larger, then one would be able to observe thermalisation happening prior to quenching. The residuals for the $P_{22}(7.5)$ line and N_2 and CO_2 in figure 71 show that CO_2 at low pressures is actually

more thermalized than N_2 despite the fact that quenching is working against this process. The overall thermalisation cross section for CO_2 then has to be greater than that for N_2. This result is consistent with a pre-laser era experiment on rotational energy transfer in NO-A-$^2\Sigma^+$ for K'=13 where it was found that CO_2 was more efficient than N_2 at inducing RET by a factor of 1.4 [76].

4.2. Extrapolation of flow cell results to the flame environments.

The three atmospheric flames studied seem to follow more closely the trends observed for CO_2 at room temperature. In general, emission spectra tend to remain peaked at the initially-pumped level with very little leaking into additional rotational levels. This agrees with the widely accepted idea that in a flame environment at atmospheric pressure quenching is by far the most important deactivation pathway [71]. Collider densities at this pressure are high and the elevated temperatures increase the collision rate by at least at factor of two or three.

The present availability of extensive quenching data for the A-$^2\Sigma^+$ state of NO [71,72,73,74] allowed us to relate the observed trend in the flame spectra to the collisional environment in the burnt-gas region of the three flames. The CHEMKIN code [108] was used to generate model predictions of the mole fractions of atomic and molecular species in a flame based on a vast kinetic rate constant data-base and modified to account for the most important reactions governing the chemistries of these three flames [109].

The purpose of this calculation is to check whether it is possible to make reasonable estimates of the overall deactivation rate constants $(1/\tau_{rad} + \Sigma_i k_{Qi}[Q_i])$ in each of these flames, and contrast these results with the extent of RET in each flame environment. Table VI shows a summary of the figures used for this purpose. An effective lifetime is quoted in the right column. This is approximately the timescale the excited state exists prior to being quenched, i.e. the time available for RET to take place. From these figures two important conclusions may be drawn. First, the H_2/O_2 and CH_4/O_2 flames share essentially the same collisional environment. Second, the CH_4/air yields an effective lifetime twice as long as that of either oxygen flame.

Table VI. Effective lifetime parameters.

Flame/Temperature	H_2O (mole fract./σ_Q)	CO_2 (mole fract./σ_Q)	N_2 (mole fract./σ_Q)	effective lifetime (ns)
CH_4/air 1933K(a)	$0.18/22\text{Å}^2$	$0.09/46\text{Å}^2$	$0.72/0.8\text{Å}^2$	2
CH_4/O_2 2554K(b)	$0.59/17\text{Å}^2$	$0.25/46\text{Å}^2$	----/1.6Å^2 (c)	1
H_2/O_2 2579K(b)	$0.884/17\text{Å}^2$	----/46Å^2 (c)	----/1.6Å^2 (c)	1

(a) experimental datum from G. P. Smith and D. R. Crosley, 18th Symposium (International) on Combustion (The Combustion Institute, Pittsburg, PA 1981) pp. 1511
(b) estimated assuming 500K cooling of the model temperature.
(c) species is either absent in the flame environment or its concentration is negligible.

In this particular calculation, temperatures for the oxygen flames had to be estimated from the model temperatures due to lack of experimental data. A cooling of 500K of the model temperature was assumed. It is reassuring that assuming 1000K cooling yields the same results. Atmospheric CH_4/air flames have been studied previously [97] and the temperature in the burnt-gas region measured was 1900K

These estimates of the effective lifetime are consistent with figure 70 where the only significant difference occurs between the CH_4/air spectra and those corresponding to the oxygen flames. Differences in collisional environments between the air and oxygen flames are not as stark as observed for N_2 and CO_2 at room temperature. This is due to two main reasons. The N_2 quenching cross section, unlike H_2O or CO_2, increases with temperature and its contribution to the overall quenching rate becomes significant, especially at atmospheric pressure [71]. Also, in spite of N_2 being the major species present (72%) there are still considerable amounts of H_2O (18%) and CO_2 (9%) which still have a significant effect on the reduction of the effective lifetime.

This section has made use of an assumption about the nature of rotational energy transfer, namely, that it is quite insensitive to temperature. Without such assumption it would have not been possible to extrapolate the flow cell results to the flame data and from there arrive at the conclusions given here, in accordance with quenching estimates of the effective lifetimes in the flames. Strictly speaking, there are no studies on the

temperature dependence of rotational energy transfer. However, a recent crossed molecular beam experiment to measure cross sections for the inelastic scattering of OH-X-$^2\Pi$ with CO and N_2 [110] showed no strong translational energy dependence of RET for either collision partner. This is consistent with a weak temperature dependence which allows us to extrapolate, at least qualitatively, from room temperature up to flame temperatures.

4.3. Rotational level dependence of rotational energy transfer.

Both the flow cell and flame data suggest a plausible rotational level dependence of the rotational relaxation rate for A-$^2\Sigma^+$ NO. N_2 has a total rotational relaxation rate of 10 Å^2 for J'=6.5 and of 2 Å^2 for J'=19.5. Analogously, the CH$_4$/air data (figure 70) shows a decreasing residual with increasing rotational level. For example, differences between the CH$_4$/air and the oxygen flames are very clear for J'=6.5 while for J'=19.5 the differences diminish and for J'=37.5 there is practically no difference between the three flames. In the same flame environment, the excited state has the same lifetime over the rotational levels pumped but the residuals are smaller for increasing rotational level. Moreover, residuals in all three cases (fig. 70) are practically indistinguishable for J'=37.5 while we know that the collisional environment is 'softer' in the CH$_4$/air case. All this suggests that the overall thermalisation cross section decreases with rotational number. Similarly, the flow cell data for N_2 shows the same features since a higher collider pressure is required for $Q_{11}(19.5)$ to thermalize than for $P_{22}(7.5)$.

The same behavior has been observed for OH in flames [46] and has been rationalized by considering the increase in spacing between rotational levels as J increases. In the light of this argument one would expect a lower dependence of RET on rotational number for NO given its smaller rotational constant compared with OH, i.e. rotational levels are more closely spaced.

There are, however, problems with this rationalization. State-to-state RET cross sections for OH-N_2 collisions [96] pumping J'=1.5 to J'=6.5 could not explain the large differences in overall RET observed for OH in flames. Similarly for NO, the data of

Quingyu et al. [100] does not seem to support this trend either for state-to-state cross sections up to J'=18.5.

Further investigation of RET in both OH and especially in NO would be of great help in elucidating whether our observations are consistent with the justification provided.

4.4. Diagnostic implications.

Everything discussed so far has important implications for the LIF diagnostics in flames as well as in other environments characterized by high temperatures and pressures.

Due to the predominance of quenching, the appearance of emission spectra is highly dependent on which rotational level is pumped. For thermometry, a standard LIF application, it is therefore necessary to ensure a sufficiently wide bandpass, i.e. 3nm in our detection scheme of the (0,1) band, in order to avoid bias over particular rotational levels. For example, narrow bandpass detection centered at the peak of the emission signal for J'=6.5, the peak of a rotational distribution at 280K, will favor detection of low-J levels, thus artificially lowering the measured temperature. There appears to be no justification for an automatic assumption that emitting states are thermalized.

Moreover, using the spectral simulation program it was possible to fit the room temperature as well as the low-J flame spectra to rotational distributions at 280-300K. Even simple physical intuition suggests that these temperatures are far from representing the thermodynamic temperature of a flame.

This last finding has important diagnostic implications of its own right. Imagine one encounters a new system of interest previously not investigated and suitable for LIF diagnostics. Furthermore, it is known that NO abounds and we decide to use emission spectra for temperature measurements. The emission spectra rersulting from pumping a low-J rotational level reveals a thermal distribution. However, and as we found in this section there is no guarantee that the temperature of the excited ensemble corresponds to the thermodynamic temperature. The reason for this has been illustrated throughout the rotational energy transfer experiments. Rotational relaxation is highly dependent on the lifetime of the excited state which at the same time is strongly correlated to the collisional

environment the excited state is exposed to. This finding might seem obvious for the case of our particular system, a flame. The issue would not turn out to be as simple for non-equilibrium systems where there is no *a priori* knowledge of the temperature.

4.5. Conclusions and future aims.

All the conclusions gathered from this study can be subdivided into two groups. First, those pertaining to the mechanism and dynamics of RET in NO A-$^2\Sigma^+$; second, those of a more direct relevance in the application of laser diagnostics to practical systems.

4.5.1. Dynamic implications.

-At room temperature N_2 was found to be efficient at overall rotational relaxation with estimated cross sections of $10\text{\AA}^2$ and $2\text{\AA}^2$ for J'=6.5 and J'=19.5 respectively. CO_2, on the contrary, was not able to induce much rotational relaxation presumably because the inefficiency of quenching. Based on this observation, it was possible to assign an upper value of $61\text{\AA}^2$ to the overall rotational relaxation cross section of CO_2. The differences between N_2 and CO_2 can be explained by considering the competition between quenching and rotational energy transfer.

-In the flame environments, all the emission spectra could be rationalized by extrapolating the room-temperature findings. Quenching predominates, which allows little RET prior to emission. Additional RET occurs in the CH_4/air flame in agreement with effective lifetime estimates using recent quenching data. The extrapolation of room temperature data to the flame data seems to be safe at least at a qualitative level. Furthermore, recent crossed-beam data seems to validate it.

-Both flow cell and flame data suggest a level-dependent rotational relaxation cross section. Cross sections decrease with rotational quantum number, as has been observed previously for the OH radical in flames. This dependence may be attributed to the increase in energy level spacing with rotational quantum number.

This study is far from being an exhaustive account of RET in NO A-$^2\Sigma^+$. Future directions in this area will have to address at least three different aspects of this energy transfer process: measurement of state-to-state cross sections, rotational-level dependence and temperature dependence.

4.5.2. Diagnostic considerations.

The experimental findings described and explained in sections 3 and 4 are relevant to all those interested in using nitric oxide for laser diagnostics. Two major conclusions are apparent from section 4.4:

- Nitric oxide excitation scans require a bandpass of at least 3 nm to avoid detection bias against particular rotational levels, which could alter the measured temperature.
- Use of emission spectra for temperature measurements should be exercised with caution. As in the nitric oxide case, spectra might appear thermal but represent a temperature that does not correspond at all with the thermodynamic temperature. This finding emphasizes the importance of knowing the characteristics of the collisional environment one is trying to probe via LIF.

Parallel to the fundamental work on RET suggested in section 4.5.1 it would be very helpful to continue the study of rotational relaxation in nitric oxide for other colliders present in environments of diagnostic interest. Such is the case for H_2O, CO, O_2 or H_2. These studies could follow the same scheme delineated in this work and would be aimed at providing useful guidance for further application of LIF diagnostics to nitric oxide.

5. References.

1. E. U. Condon and G. H. Shortley, 'The Theory of Atomic Spectra', Cambridge University Press, Cambridge, 1977.

2. P. W. Atkins, 'Physical Chemistry', 4th Ed., Freeman, New York, 1990.

3. G. Herzberg, 'Molecular Spectra and Molecular Structure I. Spectra of Diatomic Molecules', 2nd Ed., Van Nostrand Reinhold Co., 1950.

4. K. P. Huber and G. Herzberg, 'Molecular Spectra and Molecular Structure IV. 'Constants of Diatomic Molecules', 2nd Ed., Van Nostrand Reinhold Co., 1979.

5. I. Kovacs, 'Rotational Structure in the Spectra of Diatomic Molecules', Elsevier, New York, 1969.

6. D. L. Albritton, A. L. Schmeltekopf and R. N. Zare, *J. Mol. Spectrosc.*, **67**, 1976: 132.

7. R. P. Lucht, R. C. Peterson and N. M. Laurendeau, 'Fundamentals of Absorption Spectroscopy for Selected Diatomic Flame Radicals', NSF Report, 1978.

8. R. P. Wayne, 'Principles and Applications of Photochemistry', Oxford University Press, 1989.

9. A. Gilbert and J. Baggott, 'Essentials of Molecular Photochemistry', Blackwell Scientific Publications, 1991.

10. A. Schultz, H. W. Cruse and R. N. Zare, *J. Chem. Phys.* **57**, 1972: 1354.

11. M. P. Sinha, A. Schultz and R. N. Zare, *J. Chem. Phys.* **58**, 1973: 549.

12. R. N. Zare and P. J. Dagdidian, *Science* **185**, 1974: 739.

13. V. S. Letokhov et al., 'Laser Analytical Spectrochemistry', Adam Hilger, Boston, 1986

14. A. H. Zewail, *Physics Today* **33**, 1980: 33.

15. R. N. Zare, *Far. Disc. Chem. Soc.* **67**, 1979: 7.

16. A. H. Zewail, *Far. Disc. Am. Chem. Soc.* **91**, 1991: 207.

17. M. Dantus, *Comm. At. Mol. Phys.* **26**, 1991: 131.

18. G. R. Fleming, 'Chemical Applications of Ultrafast Spectroscopy', Oxford University Press, New York, 1986.

19. T. P. Dougherty, G. P. Wiederrecht, K. A. Nelson, M. H. Garrett, H. P. Jensen and C. Warde, *Science* **258**, 1992: 770.

20. A. M. Weiner, D. E. Leaird, G. P. Wierderrecht, K. A. Nelson, *Science* **247**, 1990: 1317.

21. I. C. Halalay and K. E. Nelson, *Phys. Rev. Lett.* **69**, 1992: 636.

22. A. Sengupta and M. D. Fayer, *J. Chem. Phys.* **100**, 1994: 1673.

23. D. Zimdars, A. Tokmakoff, S. Chen, S. R. Greenfield and M. D. Fayer, *Phys. Rev. Lett.* **70**, 1993: 2718.

24. L. Song, S. F. Swallen, R. C. Dorfman, K. Weidemaier and M. D. Fayer, *J. Phys. Chem.* **97**, 1993: 1374.

25. W. C. Gardiner, *Scientific American*, **246(2)**, 1982: 110.

26. G. A. Raiche, J. B. Jeffries and M. S. Brown, in *Laser Techniques for State-Selected and State-to-State Chemistry II*, ed. J. W. Hepburn, SPIE **2124**, 1994, in press.

27. G. A. Raiche and J. B. Jeffries, *Appl. Opt.* **32**, 1993: 4629.

28. G. A. Raiche and J. B. Jeffries, *Appl. Phys. Lett.* **63**, 1993: 3002.

29. J. B. Jeffries, G. A. Raiche and M. S. Brown, *Optical Diagnostics of Diamond CVD Plasmas*, paper MP94-038, Western States Meeting of the Combustion Institute, University of California at Davis, March 21-22, 1994.

30. A. W. Phelps and K. R. Stalder, *Appl. Phys. Lett.* **57**, 1990: 1090.

31. D. R. Crosley, *Local Measurement of Tropospheric HO$_x$*, SRI International Report MP92-135R, 1993.

32. D. R. Crosley, *ACS Symposium Series*, **134**, 1980: 3.

33. D. R. Crosley, *Turbulence and Molecular Processes in Combustion*, Elsevier Science Publishers B. V.: 221.

34. D. R. Crosley, *Combustion and Flame* **78**, 1989: 153.

35. G. D. Kubiak, G. O. Sitz and R. N. Zare, *J. Chem. Phys.* **83**, 1985: 2538.

36. D. C. Jacobs and R. N. Zare, *J. Chem. Phys.* **85**, 1986: 5457.

37. D. C. Jacobs, R. J. Madix and R. N. Zare, *J. Chem. Phys.* **85**, 1986: 5469.

38. R. L. Van de Wal, B. E. Holmes, J. B. Jeffries, P. M. Danehy, R. L. Farrow and D.

J. Rakestraw, *Chem. Phys. Lett.* **191**, 3-4, 1992: 251.

39. Q. Zhang, S. A. Kandel, T. A. W. Wasserman and P. H. Vaccaro, *J. Chem. Phys.* **96**, 1992: 1640.

40. S. Williams, R. N. Zare and L. A. Rahn, *Reduction of Four-Wave Mixing Spectra to Relative Populations I: Weak Field Limit*, submitted to the Journal of Chemical Physics.

41. S. Williams, R. N. Zare and L. A. Rahn, *Reduction of Four-Wave Mixing Spectra to Relative Populations I: Strong Field Limit*, submitted to the Journal of Chemical Physics.

42. D. R. Crosley, *J. Chem. Ed.* **59**, 1982: 446.

43. J. L. Kinsey, *Ann. Rev. Phys. Chem.* **28**, 1977: 349.

44. U. Westblom, F. Fernández-Alonso, G. P. Smith, D. R. Crosley and J. B. Jeffries, unpublished work.

45. D. R. Crosley, G. P. Smith, *Optical Engineering*, **22**, 1983: 545.

46. D. R. Crosley, *Optical Engineering*, **20**, 1981: 511.

47. U. Westblom, F. Fernández-Alonso, G. P. Smith, D. R. Crosley and J. B. Jeffries, *LIF Studies of Manganese Additive Effects on Low Pressure Propane Air Flames*, paper WS93-054, Western States Meeting of the Combustion Institute, SRI International, October 18-19, 1993 (see appendix I); submitted and accepted for publication in *Combustion and Flame*.

48. K. J. Rensberger, J. B. Jeffries, R. A. Copeland, K. Kohse-Höinghaus, M. L. Wise and D. R. Crosley, *Applied Optics* **28**, 1989: 3556.

49. D. E. Heard, Jay B. Jeffries, G. P. Smith and D. R. Crosley, *Combustion and Flame* **88**, 1992: 137.

50. J. M. Hollas, 'Modern Spectroscopy', Wiley, New York, 1987.

51. C. P. Fenimore, *Thirteenth Symposium (International) on Combustion*, The Combustion Institute, Pittsburg, 1971: 373.

52. D. R. Crosley, *J. Phys. Chem.* **93**, 1989: 6273.

53. T. Carrington, *J. Chem. Phys.* **35**, 1961: 807.

54. O. Stern and M. Volmer, *Z. Physik* **20**, 183: 1919.

55. F. Hund, *Zeits. f. Physik* **36**, 1926: 657.

56. I. Deézsi, *Acta Phys. Hung.* **9**, 1958: 125.

57. D. R. Crosley, *Measurement of Atmospheric Gases*, SPIE Vol. 1433, 1991: 58.

58. D. L. Andrews (editor), 'Applied Laser Spectroscopy', VCH Publishers, New York, 1992.

59. M. D. Levenson and S. S. Kano, 'Introduction to Non-Linear Laser Spectroscopy', Academic Press, Boston, 1988.

60. NASA Ref. Publication 1049, *The Stratosphere Present and Future*, R. D. Hudson and E. I. Reed Eds., 1989.

61. R. P. Wayne, 'Chemistry of Atmospheres', Clarendon Press, Oxford, 1991.

62. F. R. Gilmore, *J. Quant. Spectrosc. Radiat. Tranfer* **5**, 1965: 369.

63. R. Engleman, Jr. and P. E. Rouse, *J. Mol. Spec.* **37**, 1971: 240.

64. R. Freedman and R. W. Nichols, *J. Mol. Spec.* **83**, 1980: 223.

65. H. Scheingraber and C. R. Vidal, *J. Chem. Phys.* **83**, 1985: 3873.

66. C. O. Laux and C. H. Kruger, *J. Quant. Spectrosc. Radiat. Tranfer* **48**, 1992: 9.

67. I. S. McDermid and J. B. Laudenaslager, *J. Quant. Spectrosc. Radiat. Tranfer* **27**, 1982: 483.

68. J. R. Reisel, C. M. Carter and N. M. Laurendeau *J. Quant. Spectrosc. Radiat. Tranfer* **47**, 1992: 43.

69. M. Assher and Y. Haas, *J. Chem. Phys.* **76**, 1982: 2115.

70. Y. Haas and G. D. Greenblat, *J. Phys. Chem.* **90**, 1986: 513.

71. D. E. Heard, J. B. Jeffries and D. R. Crosley, *Chem. Phys. Lett.* **178**, 1991: 533.

72. G. A. Raiche and D. R. Crosley, *J. Chem. Phys.* **92**, 1990: 5211.

73. J. W. Thoman, J. A. Gray, J. L. Durant and P. H. Paul, *J. Chem. Phys.* **97**, 1992, 8156.

74. M. C. Drake and J. W. Ratcliffe, *J. Chem. Phys.* **98**, 1993: 3850.

75. T. Imajo, K. Shibuya, K. Obi and I. Tanaka, *J. Phys. Chem.* **90**, 1986: 6006.

76. P. Broida and T. Carrington, *J. Chem. Phys.* **38**, 1963: 136.

77. A. Melton and W. Klemperer, *J. Chem. Phys.* **55**, 1971: 1468.

78. R. G. Gordon, Y.-N. Chiu, *J. Chem. Phys.* **55**, 1971: 1469.

79. A. D. Esposti, H.-J. Werner, *J. Chem. Phys.* **93**, 1990: 3351.

80. A. Vegiri and S. C. Farantos, *Mol. Phys.* **69**, 1990: 129.

81. M. H. Alexander, A. Berning, A. D. Esposti, A. Joerg, A. Kliesch and H.-J. Werner, *Ber. Bunsenges. Phys. Chem.* **94**, 1990: 1253.

82. A. J. McCaffery, M. J. Proctor and B. J. Whitaker, *Ann. Rev. Phys. Chem.* **37**, 1986: 223.

83. J. I. Steinfield, P. Ruttenberg, G. Millot, G. Fajoux and B. Lavorel, *J. Phys. Chem.* **95**, 1991: 9638.

84. P. M. Agrawal, V. Garg and K. R. Patidar, *Acta Physica Polonica A* **84**, 1993: 257.

85. T. A. Brunner, N. Smith, A. W. Karp and D. E. Pritchard, *J. Chem. Phys.* **74**, 1981: 3324.

86. S. L. Dexheimer, M. Durand, T. A. Brunner and D. E. Pritchard, *J. Chem. Phys.* **76**, 1982: 4996.

87. L. D. Snow, R. N. Compton and J. C. Miller, *J. Chem. Phys.* **88**, 1988: 1652.

88. H. Joswig, P. Andresen and R. Schrinke, *J. Chem. Phys.* **85**, 1986: 1904.

89. G. O. Sitz and R. L. Farrow, *J. Chem. Phys.* **93**, 1990: 7883.

90. T. Carrington, *J. Chem. Phys.* **31**, 1959: 1418.

91. M. Kaneko, Y. Mori and I. Tanaka, *J. Chem. Phys.* **48**, 1968: 4468.

92. D. Kley and K. H. Welge, *J. Chem. Phys.* **49**, 1968: 2870.

93. J. I. Steinfield and W. Klemperer, *J. Chem. Phys.* **42**, 1965: 3475.

94. K. M. Evenson and H. P. Broida, *J. Chem. Phys.* **44**, 1966: 1637.

95. W. Brennen and T. Carrington, *J. Chem. Phys.* **46**, 1967: 7.

96. R. K. Lengel and D. R. Crosley, *J. Chem. Phys.* **67**, 1977: 2085.

97. G. P. Smith and D. R. Crosley, *Eigtheenth Symposium (International) on Combustion,* The Combustion Institute, 1981: 511.

98. D. R. Crosley and G. P. Smith, *Combustion and Flame* **44**, 1982: 27.

99. W. G. Mallard, J. H. Miller and K. C. Smyth *J. Chem. Phys.* **76**, 1982: 3483.

100. W. Qingyu, M. Yang and Y. Li *J. Electrochem. Soc.* **137**, 1990: 3099.

101. R. W. B. Pearse, 'The Identification of Molecular Spectra', 4th ed., Champman and

Hall, New York, 1977: 235.

102. U. Westblom, F. Fernández-Alonso, G. P. Smith, D. R. Crosley and J. B. Jeffries, unpublished work.

103. B. P. Straugham and S. Walker, 'Spectroscopy', vol. 1, Wiley and Sons, New York, 1976.

104. R. N. Zare et al., *J. Mol. Spectrosc.* **46**, 1973: 37.

105. R. J. LeRoy, *Computer Physics Communications* **59**, 1989: 383; for a copy of the simulation programs RKR1, LEVEL 5.1 and BCONT 1.4 contact: R. J. LeRoy, Guelph-Waterloo Centre for Graduate Work in Chemistry, Waterloo, Ontario N2L3G1, Canada (e-mail: leroy@theochem.uwaterloo.ca).

106. Jorge Luque Sánchez, LIFBASE emission simulation package, Laser-Based Diagnostics Group, Molecular Physics Laboratory, SRI International, 1993 (e-mail: LUQUE@MPLVAX.SRI.COM).

107. P. R. Bevington, 'Data Reduction and Error Analysis for the Physical Sciences', McGraw-Hill, New York, 1969: 18.

108. R. A. Kee, J. A. Miller and T. A. Jefferson, *Sandia National Laboratory Report SAND80-8003* (1980).

109. G. P. Smith, personal communication.

110. D. M. Sonnenfroh, R. G. MacDonald, K. Liu, *J. Chem. Phys.* **94**, 1991: 6508.

111. F. Fernández-Alonso, G. A. Raiche and D. R. Crosley, *Rotational Energy Transfer in $A^2\Sigma^+$ NO in Atmospheric Flames and Flow Cells*, paper MP 94-047, Western States Meeting of the Combustion Institute, University of California at Davis, March 21-22, 1994 (see appendix II). In preparation for submission to *Applied Optics*.

Appendices I and II.

Appendix I contains the paper presented at the Western States Meeting of the Combustion Institute in October 1993; it includes the work on the propane-air flame described in the introduction. This work has been recently submitted and accepted to be part of the next Symposium (International) on Combustion and will be published in *Combustion and Flame*.

Appendix II is a paper recently presented at the Western States Meeting of the Combustion Institute held at the University of California at Davis in March 1994. An extension to this paper is in preparation for submission to *Applied Optics*. This work has been presented at the National Conference of Undergraduate Research (NCUR '94) held in Kalamazoo, Michigan on April 14th-16th, 1994.

Appendix I: LIF Studies of Manganese Additive Effects on Low Pressure Propane-Air Flames.

Appendix II: Rotational Energy Transfer in $A^2\Sigma^+$ NO in Atmospheric Flames and Flow Cells.